Uncovering the Roles of *Mycobacterium tuberculosis melH* in Redox and Bioenergetic Homeostasis: Implications for Antitubercular Therapy

Running title: *melH* Deletion Causes Redox and Bioenergetic Imbalance

Yu-Ching Chen,[a] Xinxin Yang,[b] Nan Wang,[b] Nicole S. Sampson[b,c,#]

[a]Program in Biochemistry and Structural Biology, Stony Brook University, Stony Brook, NY 11794-5215

[b]Department of Chemistry, Stony Brook University, Stony Brook, NY 11794-3400

[c]Department of Chemistry, University of Rochester, Rochester, NY 14627-0216

[#]Corresponding author:

nicole.sampson@rochester.edu

Keywords

Mycobacterium tuberculosis, redox homeostasis, ergothioneine, aldehyde, bioenergetic homeostasis

Abstract

Mycobacterium tuberculosis (*Mtb*), the pathogenic bacterium that causes tuberculosis, has evolved sophisticated defense mechanisms to counteract the cytotoxicity of reactive oxygen species (ROS) generated within host macrophages during infection. The *melH* gene in *Mtb* and *Mycobacterium marinum* (*Mm*) plays a crucial role in defense mechanisms against ROS generated during infection. We demonstrate that *melH* encodes an epoxide hydrolase and contributes to ROS detoxification. Deletion of *melH* in *Mm* resulted in a mutant with increased sensitivity to oxidative stress, a minor increase in the bacterium's sensitivity to NO exposure. This heightened vulnerability is attributed to the increased expression of *whiB3*, subsequently leading to decreased production of mycothiol and ergothioneine. Our study elucidated profound effects on the bioenergetic metabolism of *Mm* upon disruption of *melH*. The absence of *melH* resulted in reduced intracellular levels of NAD^+, NADH, and ATP, and accumulation of aldehydes within *Mm.* Bacterial growth was impaired, even in the absence of external stressors, and was carbon-source-dependent. Taken together, these results highlight the essential role of *melH* in mycobacterial metabolism and provide new insights into the complex interplay between redox homeostasis and carbon utilization in mycobacteria.

Importance

This study unveils the pivotal role played by the *melH* gene in *Mycobacterium tuberculosis* and *Mycobacterium marinum* in combatting the detrimental impact of oxidative conditions during infection. This investigation revealed notable alterations in level of cytokinin-associated aldehyde, *para*-hydroxybenzaldehyde, as well as the redox buffer ergothioneine, upon deletion of *melH*. Moreover, changes in crucial cofactors responsible for electron transfer highlighted *melH*'s crucial function in maintaining a delicate equilibrium of redox and bioenergetic

processes. These findings collectively emphasize the potential of *melH* as an attractive target for the development of novel antitubercular therapies, offering new avenues for combating tuberculosis.

Mycobacterium tuberculosis (*Mtb*) causes tuberculosis (TB), a significant global health threat that, in 2022, was the second leading cause of death from an infectious agent after COVID-19 (1). The pathogen's metabolic flexibility is key to its success, enabling its survival in diverse and challenging environments of the human host, which impose both oxidative and reductive stresses (2). However, much remains unknown about the role of *Mtb* metabolic flexibility in maintaining redox homeostasis, which is also critical to *Mtb*'s ability to cause disease. In addition, a comprehensive understanding of the adaptive mechanisms *Mtb* employs to survive in the human host can aid in identification of innovative therapeutic strategies.

The *Mtb* H37Rv strain has at least six potential epoxide hydrolases (EHs), which belong to the virulence, detoxification, and adaptation functional category (3). EHs convert epoxides to *trans*-dihydrodiols and play a role in detoxification of xenobiotics and biotransformation of endogenous epoxides, and in signaling-molecule regulation (4). Recent evidence suggests that elucidating the function of the epoxide hydrolase B (EphB, MelH) encoded by the *melH* (*Rv1938*) gene of the *mel2* locus, which is present in *Mtb* and *Mm*, and developing small-molecule inhibitors of this enzyme could provide insights into its biological role and offer promising opportunities for drug target development (5). The *mel2* locus plays a significant role in oxidative stress resistance in *Mtb*-infected macrophages, but biochemical data regarding the locus's function have not yet been obtained (6). And study of MelH can offer insights into oxidative stress resistance and detoxification pathways.

Mtb is exposed to an increased flux of reactive oxygen species (ROS) and reactive nitrogen species (RNS) compared to its non-pathogenic counterparts, originating from its own metabolism as well as the host's defense mechanisms. However, *Mtb* has developed multiple mechanisms to effectively utilize ROS and RNS in redox reactions, enabling it to counteract the

heightened oxidative and nitrosative stresses imposed by the host's immune system. For example, *Mtb* produces two thiol couples, mycothiol (MSH) and ergothioneine (EGT), that act as major redox buffers against various redox stressors (7, 8). Moreover, the *whiB3* gene, which encodes a 4Fe-4S redox sensor and virulence protein (designated WhiB3) (9), maintains intracellular redox homeostasis to provide metabolic and cellular integrity (7, 10, 11). However, how *Mtb* regulates *whiB3* expression and EGT and MSH biosynthesis to maintain redox homeostasis is not clear.

In addition to ROS, *Mtb* has evolved the ability to endure the presence of host-generated antimicrobial molecules such as nitric oxide (NO). Recent research has revealed a connection between increased susceptibility to NO and the buildup of para-hydroxybenzaldehyde (*p*HBA) in *Mtb* mutants impaired in proteasomal degradation. However, the precise mechanism through which aldehydes render *Mtb* susceptible to this host defense remains unclear. Unraveling this mechanism could potentially uncover a broader role for aldehydes in the regulation of *Mtb* infection.

In this study, we combined metabolomic, bioenergetic, and transcriptomic approaches to evaluate how *melH* deletion impacts redox balance and bioenergetic homeostasis, which in turn moderates survival. Our investigation elucidated the critical importance of *melH* in regulating *whiB3,* maintaining EGT levels and accumulating aldehydes, suggesting a link between all three in protecting against imbalanced redox stresses and in maintaining bioenergetic homeostasis.

Results

melH-encoded protein has epoxide hydrolase activity

melH (*Rv1938*) encodes a putative epoxide hydrolase B (EphB, MelH) with an alpha/beta hydrolase domain and a cap domain (5). Recombinant *Mtb* MelH was produced and purified (Figure S1A), and its identity was confirmed by mass spectrometry. We showed that a MelH hydrolyzed the artificial fluorogenic epoxide substrate PHOME (Figure S1B). The enzyme also demonstrated epoxide hydrolase activity similar to that of the C-terminal domains of a human soluble epoxide hydrolase (sEH) but lacked phosphatase activity (Figure S1C, D) (12).

melH affects *Mtb* and *Mm* susceptibility to oxidative stress

Previous work has suggested that *mel2* locus is involved in the regulation of redox homeostasis (6, 13, 14). Through *in silico* analysis, it was discovered that among the six genes (melF-K) in the *mel2* locus of *Mm* and *Mtb*, *melF*, *melG*, and *melH* closely resemble homologs of bioluminescence-related genes, luxA, luxG, and luxH, respectively (13). The results of the study highlight the potential significance of *melF*, *melG*, and *melH* genes in the resistence of ROS-mediated oxidative stress. Here, we investigated how *mel2* gene mutations affected *Mtb*'s response to oxidative stress. Under normoxic conditions, *melF:Tn*, *melG:Tn*, and *melH:Tn* transposon mutants did not show increased ROS levels relative to the wild type (WT) in cultures grown with glycerol as sole carbon source. However, in response to potent oxidants, the *melH* mutant exhibited a significantly greater increase in ROS levels than the *melF* and *melG* mutants and wild-type (WT) *Mtb* CDC1551 (Figure 1A). The *melH* mutant also showed reduced survival rates compared to the WT and the *melF* and *melG* mutants under oxidative stress (Figure 1B). These findings suggest that *melH* plays a critical role in regulating ROS-mediated oxidative stress in *Mtb*.

Mycobacterium marinum (*Mm*) has recently proven to be an applicable model for studying TB. Most importantly, the complete *mel2* locus, exhibiting gene arrangement and transcription orientation identical to the *Mtb*, has been identified in *Mm* (Figure S2A)(13). Using NCBI Protein BLAST (BLASTp), a sequence alignment was performed between the amino acid sequences of MelH from *Mtb* and *Mm*. The result showed that the two MelH sequences share a high degree of similarity (Figure S2B). Specificially, there was 87% amino acid identity, and 94% of the aligned positions showed positive matches, suggesting high similarity of physicochemical properties and function of MelH between *Mtb* and *Mm*. To avoid any polar effects of transposition and to better understand the biochemical role of *melH* in *Mtb*'s defensive regulation of oxidative stress, we generated in frame Δ*melH* knock-out (KO) mutants and Δ*melH* complemented strains of *Mtb* and *Mm* by using specialized transduction in the clinical isolate *Mtb* CDC1551 and in *Mm* ymm1; and we validated the transformants by PCR (Figure S2C and D). First, we characterized the phenotypes of the Δ*melH Mtb* and *Mm* mutant and complemented strains (Figures 1C-F). Compared with ROS levels in WT *Mtb*, the levels in Δ*melH Mtb* were 3- to 4-fold and 2- to 3-fold higher in response to cumene hydroperoxide (CHP) and H_2O_2 treatment, respectively (Figure 1C). And the survival rate of Δ*melH* was lower than the rates of the WT and complemented strains upon treatment with CHP or H_2O_2 (Figure 1D). We observed an identical trend in *Mm* (Figure 1E and 1F). These results suggest that *Mtb* and *Mm* need *melH* to respond to ROS and to maintain redox balance.

melH deletion impairs *Mm* growth even in the absence of oxidative stress

Mtb and *Mm* are unique chronic intracellular pathogens that can catabolize glycolytic and gluconeogenic carbon sources during replication through central carbon metabolism, an ability that provides a survival advantage in nutrient-limited environments (15, 16). The use of various

carbon sources influences many physiological processes, including central carbon metabolism, oxidative stress response, virulence, and pathogenesis (17). To compare the effects of various carbon sources on WT *Mm* (ymm1) and Δ*melH Mm* metabolism, we cultured the mycobacteria in a carbon-defined minimal medium and assessed their growth rates in the presence of the various carbon sources. Δ*melH* grew more slowly than the WT strain when glycerol, propionate, cholesterol, or pyruvate was the sole carbon source (Figure 2A–C, F). Interestingly, the growth rates of the two strains were similar when they were cultured with even-chained or long-chain fatty acids as the sole carbon source (Figure 2D, E, G and K). Also, the two strains exhibited similar growth rates when cultured with fumaric acid, succinic acid, or malic acid as the sole carbon source (Figure 2H-J). We observed analogous growth phenotypes in *Mtb* (Figure S3A-E). These results suggest that *Mm* and *Mtb* adapt their carbon flux in response to the environment, and the carbon-source-dependent growth-rate decrease observed in Δ*melH* emphasizes the importance of *melH* in central carbon metabolism. Given the identical phenotypes of *melH* in both *Mtb* and *Mm*, we performed subsequent experiments in *Mm* strains to facilitate experimental throughput.

melH* deletion modulates bioenergetic functions of *Mm

In order to elucidate the molecular mechanisms underlying the carbon-source-dependent growth-rate defect and ROS-mediated oxidative damage observed in Δ*melH Mm*, we conducted untargeted metabolomics analyses of the WT, Δ*melH*, and Δ*melH* complemented strains grown in broth supplemented with glycerol, propionate, cholesterol, pyruvate, or oleic acid as the sole carbon source. The experimental design from the sample collection through data analysis is depicted in Figure S4A. The metabolites were extracted, separated by high-performance liquid chromatography, and subjected to electrospray ionization–time-of-flight mass spectrometry; and

the metabolomes were analyzed with MetaboScape®. After evaluating heatmaps of differential abundance, we conducted a decision tree analysis of m/z and retention time pairs, which revealed diverging sample clusters, with three groups mapped adjacent to each other (glycerol, propionate, cholesterol) and clearly separated from the oleic acid group (Figure S5A and S5B). Interestingly, in all groups of metabolomes, the differential abundance of metabolites between the WT and the mutant was minor. Of all the groups, the glycerol group showed the highest differential abundance between the WT and the mutant.

To gain a deeper understanding of the mechanisms linked to *melH* deficiency in *Mm*, we first selected the annotated and statistically significant metabolites observed in the tandem mass spectrometric confirmation experiments. Then we considered metabolites with an adjusted *P* value of <0.05 and a fold change of ≥|2.0| between WT and mutant for each carbon source to be differentially abundant metabolites (Figure 3A). The annotated and statistically significant metabolites were subjected to Metabolic Pathway Analysis (MetPA) (18) to assess changes in the abundance of metabolites from various biochemical pathways in Δ*melH Mm* compared to WT. The results showed the most statistically perturbed metabolic pathways to be nicotinamide metabolism, nucleotide metabolism, the citrate acid (TCA) cycle, and several amino acid biosynthesis pathways (Table 1 and Figure S6A).

NAD is of particular significance as it is a key cofactor of many amino acid metabolism pathways, glycolysis, and the TCA cycle (19-22). We measured intracellular NAD^+ and NADH concentrations in the *Mm* strains grown under various carbon source conditions to independently validate the changes observed. Compared with the WT, the Δ*melH* mutant showed significantly lower NAD^+ and NADH concentrations (~50%) in most carbon sources (Figure 4A). When cholesterol was the exclusive carbon source a minimal difference between WT and mutant was

exhibited in contrast to other carbon sources. Because the NAD^+/NADH ratio serves as a critical indicator of cellular redox status, metabolic activity and cell health (23), we next asked whether *melH* deletion affected the NAD^+/NADH ratio. Interestingly, the NAD^+/NADH ratios in the WT and mutant did not differ significantly under any of the carbon source conditions, suggesting that *melH* deletion did not drive the cells into a more-reduced state in the absence of oxidative stress (Figure 4A).

Because electron transfer reactions are the main function of NAD (20), we next determined whether the lower intracellular NAD^+ and NADH levels in the mutant might be due to increased proton conductance and resulting membrane depolarization, as seen with classical uncouplers. We used the fluorescent dye 3,3′-diethyloxacarbocyanine iodide (3) to measure the membrane potential of *Mm* cells. Δ*melH* showed no changes in membrane potential compared to WT under the tested carbon source conditions, although, as expected, the membrane uncoupler carbonyl cyanide *m*-chlorophenyl hydrazone (CCCP) did reduce the membrane potential compared to untreated mycobacteria (Figure 4B). Given this technique's limit of detection for membrane changes, we cannot rule out a membrane potential change smaller than that caused by CCCP.

In mycobacteria, ATP synthesis depends primarily on the generation of proton motive force through the electron transport chain. Inhibition of the chain alters oxidative phosphorylation and ATP production (17). To directly address the bioenergetic status of the Δ*melH Mm* mutant, we measured intracellular ATP levels using a luciferase system. Under all the tested carbon source conditions, Δ*melH* had significantly lower intracellular ATP levels than WT (Figure 4C). Overall, the intracellular ATP level in the mutant was 3- to 4-fold lower than that in WT under most of the carbon source conditions. The difference in ATP level exceeded 4-

fold when acetate, propionate, or glycerol was the sole carbon source. In contrast, a less than 2-fold difference was observed when oleic, butyric, or palmitic acid was the sole carbon source, consistent with lack of growth phenotype in even carbon-chain fatty acids. Although the NAD^+/NADH ratio is not significantly altered, the reduced levels of NAD^+ and NADH can still impact metabolic flux through redox reactions, potentially leading to decreased ATP levels. In sum, our results demonstrate that *melH* deletion lowered redox cofactor and energy storage levels in *Mm*.

Metabolomic studies of Δ*melH Mm* show aldehyde accumulation and EGT depletion

Using the established cutoffs (Figure 3A), we further identified specific metabolites that were differentially abundant in the Δ*melH* mutant relative to WT across all tested carbon sources (Figures S6B and C). We observed increased levels of *para*-hydroxybenzaldehyde (*p*HBA) (Figure 3B), isonicotinic acid, and quinolinic acid (Figure S6D) and decreased levels of EGT (Figure 3C), L-acetylcarnitine, and tetrahydrofurfuryl butyrate (Figure S6D) in Δ*melH* relative to WT across all media.

The increase in *p*HBA observed in Δ*melH* compared to WT (Figure 3D and E) varies depending on the carbon source, with an approximately 2-fold increase in cholesterol or pyruvate medium, and approximately a 4-fold elevation in glycerol or oleic acid medium. The highest increase was observed in propionate medium, with approximately a6-fold increase in the mutant compared to WT. Additionaly, in Δ*melH*, we observed significant reductions in the levels of EGT in comparison to WT (Figure 3F and G). Specifically, EGT levels were decreased by approximately 10-fold when cholesterol was used as sole carbon source. When glycerol served as sole carbon source, EGT levels were reduced by about 3-fold. Similarly, in the presence of

propionate, oleic acid, or pyruvate as sole carbon source, Δ*melH* showed a decrease in EGT levels, with an approximately 2-fold reduction in each case.

Aldehydes accumulate in Δ*melH*

Darwin and coworkers have reported that adenine-based cytokinins and theirdegradation products, in particular *p*HBA, accumulate in an *Rv1205* mutant that sensitizes mycobacterial cells to NO (24-27). Given the accumulation of *p*HBA in Δ*melH Mm*, we examined the overall intracellular aldehyde levels in Δ*melH Mm*. Because aldehydes are inherently reactive and exist in different hydration states, their detection by mass spectrometry can be challenging. Therefore, we used a fluorgenic substrate that reacts with a broad range of aldehydes (28, 29). We measured intracellular aldehyde concentrations in *Mm* grown in glycerol, propionate, cholesterol, oleic acid, or pyruvate as the sole carbon source (Figure 5A). To ensure our assay was specific for aldehydes and not other reactive electrophiles, we tested glycidyl ether, an epoxide, as a control, and confirmed that epoxide does not react with the fluorogenic reagent.

Δ*melH* showed significantly higher aldehyde concentrations when grown in glycerol, propionate, or cholesterol compared to the WT *Mm* and the Δ*melH* complemented strains. There were slightly higher, statistically insignificant concentrations of aldehyde in the mutant when grown in pyruvate; and no difference was observed when *Mm* was grown in oleic acid (Figure 5B). These results suggest that *melH* mutation alters aldehyde metabolism..

To explore further the role of MelH with respect to intracellular aldehyde concentrations, we determined whether exogenous recombinant MelH protein could prevent aldehyde generation in WT or Δ*melH Mm* cultured with propionate as the sole carbon source. We found that exogenous recombinant MelH depleted aldehyde concentrations in cell lysates of both strains, whereas heat-denatured recombinant MelH had no effect (Figure 5C).

In a subsequent experiment, we sought to investigate whether the accumulated aldehydes observed in the Δ*melH Mm* mutant were due to aldehyde-containing compounds serving as direct substrates for MelH or if MelH might function to eliminate an aldehyde precursor present in cell lysates. To address this question, we heat denatured cell lysates, and then added purified MelH protein to these cell lysates. If the accumulated aldehyde levels were solely due to the absence of catalytically-active MelH that formed aldehyde-containing compounds as its enzymatic product, then the addition of active MelH to the denatured lysate should have reduced the aldehyde concentrations. However, we observed that the aldehyde levels remained unchanged after the addition of MelH to denatured cell lysates (Figure 5D). This result strongly suggested that MelH's direct substrate is not an aldehyde. Rather aldehydes are formed enzymatically from an unknown catalytic activity present in cell lysates and this enzymatic pathway utilizes as its substrate a metabolite that is depleted by addition of MelH epoxide hydrolyase catalyst to the cell lysate. This metabolite may be an epoxide or a precursor metabolite. In the absence of functional MelH in the Δ*melH Mm* mutant, these epoxides or precursors accumulate, and upon cell lysis, the aldehydes continue to be formed unless MelH is exogenously added to remove the epoxide/precursor. These results suggest a possible connection between MelH epoxide hydrolase activity and detoxification of intracellular aldehyde accumulation.

Aldehyde accumulation minimally sensitizes Δ*melH* to NO

We next tested if aldehyde accumulation correlated with increased susceptibility of the Δ*melH Mm* mutant to NO. *Mm* cells were exposed to acidified nitrite, a source of NO (30, 31). We observed that the nitrosative-stress-induced changes in nitrite concentration between the WT and the *ΔmelH* strain were slightly higher in the mutant, however, the differences were not statistically significant (Figure S7A). We also determined whether *melH* deletion reduced

mycobacterial survival in *Mm* compared to WT upon induction of RNS. Acidified $NaNO_2$ caused cell death at 30 min post-exposure as compared to unstressed bacteria; but the Δ*melH* survival rate was only slightly lower than the WT survival rate (Figure S7B). As expected, complementation restored Δ*melH* survival in response to acidified $NaNO_2$. We also tested the effects of *S*-nitroso-N-acetylpenicillamine (SNAP) on the survival of the three strains and found that Δ*melH* was insignificantly more sensitive to SNAP than WT or the complemented strain. These results demonstrate that *melH* is not likely to be a major contributor to NO resistance in *Mm*.

whiB3 **regulates MSH and EGT production in response to oxidative stress**

Mtb whiB3, an intracellular redox sensor, has been shown to regulate EGT production in a carbon-source-dependent manner (7). EGT and MSH are the major redox buffer present in *Mtb* and Steyn and coworkers established that EGT and MSH are both required for maintaining redox balance and bioenergetic homeostasis, which influences drug susceptibility and pathogenicity (7). Our metabolomics analysis revealed that *melH* significantly decreased EGT levels regardless of the carbon source. Therefore, we compared the transcript levels for MSH and EGT biosynthesis genes MMAR_5212 (*egtD*), MMAR_5215 (*egtA*) and MMAR_0812 (*mshA*) as well as *whiB3 whiB3* (MMAR_1132) in the Δ*melH Mm* mutant relative to WT (32, 33) using quantitative real-time PCR.

Regardless of carbon source, deletion of *melH* resulted in an approximately two-fold upregulation of *whiB3* transcription compared with that in WT under normoxic conditions (Figure 6A). Our results showed that expression of *whiB3* was upregulated six to ten-fold in Δ*melH* compared with that in the WT when the mycobacteria were grown in glycerol, propionate, cholesterol, pyruvate, or oleic acid culture and treated with oxidative stressors.

Upon exposure of *Mm* to CHP or H_2O_2, expression of *mshA*, *egtA*, and *egtD* was significantly lower in the mutant than in the WT (Figure 6B–D, respectively). Notably, when glycerol or propionate was the sole carbon source, the reduction in *egtA* expression in the CHP- or H_2O_2-treated mutant was more pronounced than the reduction observed under the other carbon source conditions. We observed significantly lower *mshA* expression in the Δ*melH* mutant than in the WT, particularly under oxidative stress conditions. Taken together, these results establish that *melH* deletion results in induction of *whiB3* expression and suggests that increased *whiB3* expression downregulates the expression of EGT and MSH biosynthesis genes.

Δ*melH Mm* failure to maintain intracellular redox homeostasis is independent of carbon source

We examined the effect of *melH* deletion on redox homeostasis in *Mm* grown with different carbon sources and found that *melH* deletion resulted in increased ROS accumulation in response to oxidative stress regardless of carbon source. Specifically, Δ*melH* exhibited an approximately 1.5- to 3-fold increase in ROS production in response to CHP or H_2O_2 treatment across all carbon sources. Interestingly, the results do not show a significant change in the ROS production in Δ*melH* compared to the WT and the complemented strains under non-stressing growth conditions. (Figure 7A).

To determine the impact of *melH*-mediated ROS toxicity on cellular survival, we measured CFUs after treatment of *Mm* cells with CHP or H_2O_2. We found that the survival rate of Δ*melH Mm* was significantly lower than the WT survival rate and that complementation of the mutant with the *mel2* operon restored intracellular survival to near WT levels across all carbon source growth conditions. (Figure 7B). Altogether, the high expression of *whiB3* exhibited under CHP- or H_2O_2-induced oxidative stress conditions in Δ*melH* is consistent with the increased

ROS levels and the decreased survival of the Δ*melH* mutant. In sum, the heightened accumulation of ROS in the mutant strain has a detrimental effect on its survival rate when exposed to an external oxidative stress. The increased ROS levels further disrupt the delicate balance of cellular redox homeostasis, overwhelming the antioxidant defense mechanisms of the mutant (Figure 8).

Discussion

In this study, our investigations unveiled that *melH* deletion primarily heightened mycobacterial susceptibility to oxidative stress conditions resulting in cell death. In contrast, *melH* deletion only slightly incresed the bacterium's sensitivity to NO exposure. Importantly, *melH* deletion disrupts coordination between ROS detoxification and thiol homeostasis, two metabolic functions required for survival during macrophage infection. The distinct physicochemical properties of low-molecular-weight thiols such as EGT and MSH, including their different reduction potentials, enable them to respond differently to a range of stresses, thereby facilitating successful infection (8). Significantly, EGT is resistant to auto-oxidation, and predominantly exists in its thione form rather than the thiol form. This unique characteristic provides EGT with exceptional stability compared to other thiols like glutathione and MSH (34). These differences of EGT and MSH likely explain our inability to detect MSH metabolite in our metabolomics data across four tested carbon source conditions (excluding glycerol). Further, we observed reduced intracellular levels of NAD^+, NADH, and ATP and accumulation of aldehydes within *Mm* upon *melH* deletion. These data point toward a role for MelH as an epoxide hydrolase that prevents the buildup of intracellular aldehydes. An unanswered question is whether *whiB3* regulation of MSH and EGT production in response to oxidative stress is a consequence of aldehyde accumulation or a direct role of *melH* in redox homeostasis. Darwin and coworkers demonstrated that accumulation of adenine-based cytokinins, eg, topolin, results in accumulation of cytokinin breakdown products like *p*HBA. Accumulation of *p*HBA is responsible for NO and Cu sensitivity in *Mtb* mutants with defects in proteasomal degradation (25-27, 35). In their RNA-Seq comparisons of WT *Mtb* treated with *p*HBA vs untreated WT, *p*HBA exhibited no influence on the expression of *whiB3*, *egtA*, *egtD*, and *mshA* genes. However, *p*HBA treatment resulted in

reduced *melH* expression (1.8-fold) in WT *Mtb. Mtb* employs various transcriptional regulators to respond to ROS and RNS, often by activating sigma factors (SigH and SigE), two-component systems (SenX-RegX and DosR/S/T), and serine-threonine kinases (PknG)(9). Darwin and coworkers' transcriptional data indicated that *p*HBA treatment did not result in significant alterations in the expression of these genes. These collective findings underscore the necessity for a more comprehensive characterization of the effects of aldehydes on cellular metabolism and gene expression.

Although our metabolomics analysis did not reveal high accumulation of any aldehydes other than *p*HBA under any of the five tested carbon source conditions, it is important to note that aldehydes can be volatile, may exist in hydrated forms, and are reactive electrophiles, which may explain why we did not observe accumulation of other aldehyde species by mass spectrometry. Although we did not observe obvious accumulation of other metabolites in the cytokinin pathway, we found accumulation of quinolinic acid (QA) and adenine in Δ*melH Mm* (Figure S6). 2-amino-3-carboxymuconate-semialdehyde, an unstable compound can be non-enzymatically transformed to QA, which is a product of tryptophan degradation and may serve as a precursor for NAD^+ (36). This finding implies a potential connection between *melH* deletion and perturbations in adenine metabolism, which may have broader implications for nucleotide biosynthesis and energy metabolism in the mutant strain.

These collective observations suggest an intricate narrative: *melH* deletion might culminate in heightened epoxide levels, thus activating *whib3* expression, WhiB3 then sensitizes mycobacteria to oxidative stress. Furthermore, this observation suggests a potential link between *melH* deficiency and alterations in cytokinin signaling, possibly impacting aldehyde accumulation.

Collectively, these studies reveal the pivotal role of *melH* in attenuating mycobacterial sensitivity to host-generated ROS and RNS. This research sets the stage for future investigations into the role of *melH* and its interactions with other pathways in mycobacterial metabolism and pathogenesis and the role of aldehyde accumulation. Here, we underscore the potential of MelH as a compelling drug target for efficaciously addressing *Mtb* infections through a novel therapeutic strategy.

Materials and Methods

Bacterial strains and culture conditions

The *melF:Tn* (NR-13643), *melG:Tn* (NR-13645), and *melH:Tn* (NR-18002) *Mtb* CDC1551 strains were obtained from BEI Resources (www.beiresources.org); and the ymm1 *Mm* strain was kindly provided by Dr. Jeffrey D. Cirillo. *Mtb* and *Mm* strains were grown at 37°C and 30 °C, respectively, in Middlebrook 7H9 medium (Difco) supplemented with 0.2% glycerol or 0.1 mM cholesterol, 0.5% bovine serum albumin, 0.08% NaCl, and 0.05% (volume/volume) tyloxapol (Sigma-Aldrich) or in Middlebrook 7H11 agar supplemented with 10% oleate-albumin-dextrose-NaCl (OADC) and 0.5% glycerol. If necessary, cultures were supplemented with sodium acetate, succinic acid, fumaric acid, butyric acid, malic acid, or palmitic acid to a final concentration of 50 μM as sole carbon source. The *melF:Tn*, *melG:Tn*, and *melH:Tn* CDC1551 strains were grown in the presence of 30 μg/mL kanamycin, whereas the Δ*melH Mtb* CDC1551 and Δ*melH Mm* ymm1 strains were grown in the presence of 50 μg/mL hygromycin B. All complemented strains were grown in the presence of 50 μg/mL hygromycin and 50 μg/mL kanamycin. For determination of the effect of the carbon source on *melH* function, *Mtb* and *Mm* were cultured in Middlebrook 7H9 medium supplemented with 10% OADC, 0.05% tyloxapol, and one of the following carbon sources: glycerol, sodium propionate, sodium pyruvate, cholesterol, oleic acid, sodium acetate, succinic acid, fumaric acid, butyric acid, malic acid, or palmitic acid to a final concentration of 50 μM.

Cloning of Δ*melH* and Δ*melH* complemented strains of *Mtb*

Δ*melH Mtb* was generated through recombinase-mediated recombination of a hygromycin-resistance cassette PCR product flanked by sequences homologous to the ~545-bp

regions upstream and downstream of the *melH* (*Rv1938*) gene. *Mtb* CDC1551 cells were transformed with an episomal plasmid containing the RecET recombinase (pNit-recET-sacB-kanR) and were induced to express the recombinase by addition of isovaleronitrile (final concentration, 1 μM) for 24 h followed by addition of glycine (final concentration, 0.2 M) for 16 h. The electrocompetent cells prepared from the induced culture were transformed with 1 μg of PCR product and were recovered for 24 h in 7H9 medium supplemented with 1 mM L-arginine. The transformants were selected on Middlebrook 7H10 agar containing 0.5% glycerol, 10% OADC, 50 μg/mL hygromycin, and 1 mM L-arginine and were validated by PCR. The validated strains were streaked on 7H11 agar supplemented with 0.5% glycerol, 10% OADC, 1 mM L-arginine, and 8.5% sucrose to select for clones that had lost the pNit-recET-sacB-kanR plasmid. The sucrose-resistant colonies were patched first onto 7H11 agar supplemented with 0.5% glycerol, 10% OADC, 1 mM L-arginine, and 30 μg/mL kanamycin and then onto the same agar without kanamycin. The kanamycin-sensitive strains were grown in 7H9 medium supplemented with 50 μg/mL hygromycin and 1 mM L-arginine to obtain the final Δ*melH Mtb* strain. For complementation of Δ*melH* strain, the target gene with a native promoter corresponding to 200-bp upstream of the first gene in the corresponding putative operon was cloned into a pMV306 integrating plasmid. The resulting construct was electroporated into the Δ*melH* mutant, and kanamycin-resistant transformants were selected.

Cloning of Δ*melH* and Δ*melH* complemented strains in *Mm*

The predicted *melH* (MMAR_2866) gene and its flanking genomic regions, as annotated in the MycoBrowser portal, were amplified by PCR using *Mm* genomic DNA. The resulting upstream and downstream amplicons were fused by PCR with the primers listed in Table S1 and the fused PCR product was purified and digested with the *Hind*III restriction enzyme (New

England BioLabs, Ipswich, MA) according to the manufacturer's instructions. The *Hind*III-linearized p1NIL plasmid (Addgene plasmid number 20187) was ligated with the *Hind*III-digested PCR product, and the ligation mixture was introduced into *Escherichia coli* DH5α. Colonies bearing the p1NIL plasmid with the *melH* flanking regions from the *Mm* genome were selected on LB agar supplemented with kanamycin, and the sequence of the resulting p1NIL-*melH* plasmid was confirmed by DNA sequencing analysis. To construct the final suicide vector for allelic exchange, we introduced the p1NIL-*melH* plasmid with the pGOAL19 cassette (Addgene plasmid number 20190) using the protocol described by Parish and Stoker (37). The presence of the pGOAL19 cassette in the p1NIL-*melH* construct was confirmed by restriction digestion. The constructed plasmid was transformed into WT *Mm* by electroporation at 2500 mV, 1000 Ω, and 25 μF; and the *Mm* deletion mutant was selected after two rounds of homologous recombination, as previously described (37). Unmarked deletion mutants with in-frame deletions were obtained after two rounds of homologous recombination. Each transformed *Mm* mutant was cultured on 7H11 supplemented with 50 mg/L hygromycin for 2 weeks, and the single colony was then subcultured on 7H11 with 100 mg/L X-gal and 50 mg/L hygromycin for 1 week to select the single cross-over transformants (blue colonies). The blue colonies were selected and cultured on 7H11 supplemented with 2% sucrose and 100 mg/L X-gal for 1 week to obtain the deletion mutant.

Central metabolite extraction

Mycobacteria were grown to an OD600 of 1.0. Approximately 1×10^8 cells were collected by filtration on 0.22-μm nylon/polyvinylidene fluoride filters (Millipore GVWP02500) and transferred to 7H11 supplemented with 0.4% glycerol, sodium propionate, cholesterol, sodium pyruvate, or oleic acid as the sole carbon source. Plates were incubated for 6 days at 30

or 37 °C for bacterial replication and biomass production. The polar metabolites were extracted in prechilled (−40 °C) 2:2:1 methanol/acetonitrile/water, and cells were lysed six times by bead-beating for 30 s with incubation on ice for 30 s between pulses. Soluble extracts were filtered (Spin-X filter tubes) at 5000g for 5 min at 4 °C and then stored at −80 °C for liquid chromatography–mass spectrometry. The bacterial biomass of each sample was determined by measuring the residual protein content in the metabolite extracts.

Metabolome analysis by liquid chromatography–mass spectrometry

The sample extract was fractionated by an Agilent 1290 Infinity II system equipped with 1) a Zorbax Eclipse Plus C18 column (1.8 µm; 2.1 by 50 mm) or 2) an InfinityLab Poroshell 120 HILIC-Z column (2.7 µM; 2.1 by 100 mm), or 3) a HiPlex H column (4.6 x 250mm, Agilent). For 1), reversed-phase separation was achieved using a gradient from solvent A (95% water, 5% acetonitrile, 0.1% formic acid) to solvent B (acetonitrile, 0.1% formic acid) as follows: 100% A held for 1.2 min, 100% B in 20.8 min, 100% B held for 1 min, 100% A in 0.1 min, and re-equilibration for 3 min (total run time, 26 min/sample). The flow rate was maintained at 200 µL/min for the duration of the run, the column was held at 35°C, and samples were held at 4°C. For 2) HILIC mode, separation was achieved for positive mode using a gradient from solvent A (10mM ammonium acetate in water) to solvent B (90% acetonitrile, 10% water, 10mM ammonium acetate) as follows: 98% B held for 0.8 min, 75% B in 19.2 min, 0% B in 3 min and held for 1 min, 98% B in 0.1 min, and re-equilibration for 3 min (total run time, 27 min/sample); For negative mode, separation was achieved using a gradient from solvent A (20 mM ammonium acetate in water, pH 9) to solvent B (acetonitrile) as follows: 100% B held for 0.8 min, 70% B in 17.2 min, 40% B in 4 min, 0% B in 1 min and held for 1 min, 100% B in 0.1 min, and re-equilibration for 3 min (total run time, 27 min/sample). The flow rate was maintained at 250

μL/min for the duration of the run, the column was held at 35°C, and samples were held at 4°C. For 3) HIPLEX mode, isocratic separation was achieved via flushing solvent at 200 μL/min (0.01% formic acid, 20% acetonitrile in water) for 20 minutes. The column was held at 50 °C. The column eluate was infused into a Bruker Impact II QTOF system with an electrospray ion source. Data were collected in both positive (A) and negative (B) ion mode, with the following settings: (A) Capillary voltage of 4,500 V; endplate offset of 500V; nebulizer gas pressure of 1.8 bar; dry gas flow rate of 8.0 L/min; dry temperature of 220 °C; MS spectra acquisition rate of 8 Hz; and m/z range of 50 to 1,500 Da). (B) Capillary voltage of 4,200 V; endplate offset of 500V; nebulizer gas pressure of 2.0 bar; dry gas flow rate of 8.0 L/min; dry temperature of 210 °C; spectra acquisition rate of 8 Hz; and m/z range of 50 to 1,500 Da).

Analysis of metabolomics data

The data were analyzed using the Bruker Compass MetaboScape® 2022b software (V9.0.1, Bruker Daltonics). Ion chromatograms were aligned, and high-resolution mass were re-calibrated using sodium formate clusters as reference mass. The metabolites were identified by comparing the accurate m/z (mass tolerance < 5 ppm) with libraries including HMDB library, Mtb LipidDB library and MycoMass library, and the MS/MS spectra with libraries including MetaboBASE Personal Library (Bruker), MSDIAL library, and HMDB library. Then the average peak intensities and the standard deviations from three biological replicates were calculated. Pathway map was plotted using *Mycobacterium tuberculosis* H37Rv metabolic map diagram (Biocyc.org). MetaboAnalyst (V5.0) was used to support metabolic pathway analysis (integrating pathway enrichment analysis and pathway topology analysis).

Determination of *Mtb* and *Mm* susceptibility to oxidants

WT *Mtb* (CDC1551); *melF:Tn*, *melG:Tn*, *melH:Tn*, and Δ*melH Mtb*; WT ymm1 and Δ*melH Mm*; and their respective complemented strains were exposed to CHP or H_2O_2. The strains were grown to 0.6–0.8 OD_{600} in 7H9 medium supplemented with 0.4% glycerol or sodium propionate. For each strain, 2×10^6 cells were transferred into each well of a 96-well plate. H_2O_2 (10 mM) or CHP (5 mM) was added to the wells, and the plates were incubated at 37 °C for 30 mins. Control cells (1×10^6) were not treated with either oxidant. The treated cells were subsequently plated on 7H11 agar plates supplemented with 10% OADC. Colonies were enumerated after 3 weeks of incubation at 37 °C. The survival of the mycobacterial strains was expressed as percentage survival relative to mycobacterial strains with no treatment.

Measurement of endogenous ROS in *Mtb* and *Mm*

Exponentially growing WT *Mtb* (CDC1551); *melF:Tn*, *melG:Tn*, *melH:Tn*, and Δ*melH Mtb*; WT ymm1 and Δ*melH Mm;* and their respective complemented strains cultured in 7H9 medium supplemented with 0.4% glycerol or sodium propionate were treated with CellROX Green (Life Technologies; final concentration, 5 μM) for 30 min at 37 °C. The cells were pelleted, and the supernatant was discarded. The cells were washed with 7H9 medium to remove any extracellular CellROX Green. The washed cells were resuspended in medium and analyzed on a plate reader at excitation/emission wavelengths of 485/565 nm.

Measurement of change in membrane potential

The changes in membrane potential of WT ymm1 *Mm*, Δ*melH Mm,* and the Δ*melH* complemented strain were determined using a BacLight Bacterial Membrane Potential Kit (ThermoFisher Scientific) according to the manufacturer's instructions. In short, 1 mL aliquots of culture at an OD_{600} of 0.8 were treated with 3,3′-diethyloxacarbocyanine iodide (3 mM) and

then CCCP (20 mM). DMSO-treated and -untreated bacilli were used as controls. Aliquots were incubated for 30 min before analysis on a plate reader.

Measurement of total ATP content

Whole cell pellet samples were collected from *Mm* cell cultures, aliquots of the suspensions were removed from the samples, and the sample was mixed with 3 mL of boiling Tris-EDTA (100 mM Tris, 4 mM EDTA, pH 7.75). Then the bacterial cells were lysed for 2 min with glass beads, heated at 100 °C for 5 min, and cooled on ice. Cellular debris was removed by centrifugation. Supernatants were collected, an equal volume of luciferase reagent (ATP Bioluminescence Assay Kit HS II, Roche) was added to each supernatant, and luminescence was measured. ATP reaction mixing and ATP measurement were performed with an ATP Colorimetric/Fluorometric Assay Kit (BioVision Research Products, Milpitas, CA) according to the manufacturer's protocol.

NADH and NAD^+ Determination

Mm Cells were rapidly harvested (two 2-mL samples) and resuspended in 0.2 M HCl (for NAD^+ determination) or 0.2 M NaOH (for NADH determination). The tubes were centrifuged at 12,535 x*g* for 1 min. The supernatant was removed, and the pellets were suspended in 300 mL of 0.2 M HCl (for NAD^+ extraction) or 0.2 M NaOH (for NADH extraction). The resulting suspensions were placed in a 50 °C water bath for 10 min and then on ice to cool them to 0 °C. The extracts were then neutralized with 300 mL of 0.1 M NaOH (for NAD^+ extraction) or 300 mL of 0.1 M HCl (for NADH extraction) added dropwise while vortexing. Cellular debris was removed by centrifuging at 12,535 x*g* for 5 min. Supernatants were transferred to new tubes, and intracellular NADH and NAD^+ concentrations were measured by means of a very sensitive cycling assay (38). The assay was performed with a reagent mixture consisting of equal volumes

of 1.0 M bicine buffer (pH 8.0), absolute ethanol, 40 mM EDTA (pH 8.0), and 4.2 mM 3-[4,5-dimethylthiazol-2-yl]-2,5-diphenyltetrazolium bromide and twice the volume of 16.6 mM phenazine ethosulfate, which had previously been incubated for 10 min at 30 °C. The following volumes were added to 1 mL cuvettes: 50 μL of neutralized extract, 0.3 mL of water, and 0.6 mL of the above-described reagent mixture. The reaction was started by adding 50 μL of yeast Alcohol dehydrogenase II (500 or 100 U/mL in 0.1 M bicine buffer [pH 8.0]). The absorbance at 570 nm was recorded for 10 min at 30 °C.

Quantitative real-time PCR

Total RNA was extracted from *Mm* cells using the TRIzol Reagent (Takara, Japan). cDNA was synthesized using a PrimeScript reverse transcriptase reagent kit (Takara, Japan). mRNA expression was examined by quantitative real-time PCR using iTaq Universal SYBR Green Supermix (Bio-Rad) and a LightCycler480 detection system (Roche, Mannheim, Germany). The relative expression of indicated genes was analyzed by the 2-ΔΔCt method. For comparisons between WT and Δ*melH Mm*, the induction ratio for each gene was normalized to *Mm* 16s rRNA expression. The primer sequences used for PCR are listed in Table #S1.

Nitrite measurement

The *Mm* cells were treated with acidified $NaNO_2$ and SNAP, and 30 min later, the Griess reagent system was used to determine levels of nitric oxide production. NO_2^- was determined by using $NaNO_2$ as a standard. Briefly, 50 μL of each experimental sample was added to wells, and then 50 μL of 1% sulfanilamide in 5% phosphoric acid was added to each experimental sample and to wells containing the dilution series for the nitrite standard reference curve. Then 50 of μL of 0.1% aqueous *N*-1-napthylethylenediamine dihydrochloride was added to each well. Absorbance was measured at 550 nm immediately after addition of the reagents to the samples.

The cells were subsequently plated on 7H11 agar supplemented with 10% OADC. Colonies were enumerated after 3 weeks of incubation at 37 °C. The survival of mycobacterial strains was expressed as percentage survival relative to mycobacterial strains with no treatment.

Aldehyde measurement

Aldehyde reaction mixing and Aldehyde concentration measurements were performed with a Fluorometric Aldehyde Assay Kit (MilliporeSigma, cat. no. MAK141), which uses a fluorogenic dye that reacts with aldehydes to generate a fluorometric product, according to the manufacturer's protocol.

Statistics

Statistical computations were performed with GraphPad Prism (ver. 9.0). Pairwise comparisons were performed using Student's *t* test for normally distributed data. Multiple comparisons were performed using the one-way analysis of variance module of GraphPad.

Supplementary materials

The following material is available online. Supplemental Table, Figures and Methods.

Data availability

Metabolomics datasets from this study are deposited in the Global Natural Products Social Molecular Networking (GNPS; http://gnps. ucsd.edu) under reference MassIVE #MSV000092681. The data that support the findings of this study are available either within this article and its supplementary information files or upon reasonable request to the corresponding author.

Author contributions

Yu-Ching Chen: Conceptualization, Methodology, Validation, Formal analysis, Investigation, Software, Data curation, Writing-Original Draft, Visualization. Xinxin Yang: Conceptualization, Methodology, Formal analysis, Supervision (Microbiology activities). Nan Wang: Methodology, Formal analysis, Software (Suggested and demoed the use of MetaboAnalyst), Supervision (Mass Spec activities). Nicole Sampson: Conceptualization, Resources, Writing-Review & Editing, Supervision, Funding acquisition.

Acknowledgements

This work was supported by NIH grant R01AI134054. The metabolomic experiments were conducted at the Stony Brook CASDA Mass Spectrometry Center. The authors would like to thank Dr. Jeffrey D. Cirillo for generously providing the ymm1 *Mm* WT strain as a gift. The authors would like to thank Dr. Tianao Yuan for valuable discussions. Special thanks to Dr. Xuejun Peng for metabolomics advice. Shearson Editorial Services (Cornwall, NY, USA) provided English language editing of the text of this paper.

References

1. WHO. 2022. Global Tuberculosis reports 2022. Geneva: World Health Organization.
2. Yuan T, Sampson NS. 2018. Hit generation in TB drug discovery: from genome to granuloma. Chem Rev 118:1887-1916.
3. Madacki J, Kopal M, Jackson M, Kordulakova J. 2021. Mycobacterial epoxide hydrolase EphD is inhibited by urea and thiourea derivatives. Int J Mol Sci 22:2884.
4. Madacki J, Laval F, Grzegorzewicz A, Lemassu A, Zahorszka M, Arand M, McNeil M, Daffe M, Jackson M, Laneelle MA, Kordulakova J. 2018. Impact of the epoxide hydrolase EphD on the metabolism of mycolic acids in mycobacteria. J Biol Chem 293:5172-5184.
5. Biswal BK, Morisseau C, Garen G, Cherney MM, Garen C, Niu C, Hammock BD, James MN. 2008. The molecular structure of epoxide hydrolase B from *Mycobacterium tuberculosis* and its complex with a urea-based inhibitor. J Mol Biol 381:897-912.
6. Cirillo SL, Subbian S, Chen B, Weisbrod TR, Jacobs WRJ, Cirillo JD. 2009. Protection of *Mycobacterium tuberculosis* from reactive oxygen species conferred by the *mel2* locus impacts persistence and dissemination. Infect Immun 77:2557-2567.
7. Saini V, Cumming BM, Guidry L, Lamprecht DA, Adamson JH, Reddy VP, Chinta KC, Mazorodze JH, Glasgow JN, Richard-Greenblatt M, Gomez-Velasco A, Bach H, Av-Gay Y, Eoh H, Rhee K, Steyn AJC. 2016. Ergothioneine maintains redox and bioenergetic homeostasis essential for drug susceptibility and virulence of *Mycobacterium tuberculosis*. Cell Rep 14:572-585.
8. Kumar A, Farhana A, Guidry L, Saini V, Hondalus M, Steyn AJC. 2011. Redox homeostasis in mycobacteria: the key to tuberculosis control? Expert Rev Mol Med 13:e39.

9. Mehta M, Singh A. 2019. *Mycobacterium tuberculosis* WhiB3 maintains redox homeostasis and survival in response to reactive oxygen and nitrogen species. Free Radic Biol Med 131:50-58.

10. Saini V, Farhana A, Steyn AJC. 2012. *Mycobacterium tuberculosis* WhiB3: a novel iron-sulfur cluster protein that regulates redox homeostasis and virulence. Antioxid Redox Signal 16:687-697.

11. Pacl HT, Reddy VP, Saini V, Chinta KC, Steyn AJC. 2018. Host-pathogen redox dynamics modulate *Mycobacterium tuberculosis* pathogenesis. Pathog Dis 76:fty036.

12. Cronin A, Mowbray S, Durk H, Homburg S, Fleming I, Fisslthaler B, Oesch F, Arand M. 2003. The N-terminal domain of mammalian soluble epoxide hydrolase is a phosphatase. Proc Natl Acad Sci U S A 100:1552-1557.

13. Subbian S, Mehta PK, Cirillo SL, Cirillo JD. 2007. The *Mycobacterium marinum mel2* locus displays similarity to bacterial bioluminescence systems and plays a role in defense against reactive oxygen and nitrogen species. BMC Microbiol 7:4.

14. Yang X, Yuan T, Ma R, Chacko KI, Smith M, Deikus G, Sebra R, Kasarskis A, Bakel HV, Franzblau SG, Sampson NS. 2019. Mce3R stress-resistance pathway is vulnerable to small-molecule targeting that improves Tuberculosis drug activities. ACS Infect Dis 5:1239-1251.

15. Rhee KY, de Carvalho LP, Bryk R, Ehrt S, Marrero J, Park SW, Schnappinger D, Venugopal A, Nathan C. 2011. Central carbon metabolism in *Mycobacterium tuberculosis*: an unexpected frontier. Trends Microbiol 19:307-314.

16. Cumming BM, Steyn AJC. 2015. Metabolic plasticity of central carbon metabolism protects mycobacteria. Proc Natl Acad Sci U S A 112:13135-13136.

17. Lamprecht DA, Finin PM, Rahman MA, Cumming BM, Russell SL, Jonnala SR, Adamson JH, Steyn AJC. 2016. Turning the respiratory flexibility of *Mycobacterium tuberculosis* against itself. Nat Commun 7:12393.

18. Xia J, Wishart DS. 2010. MetPA: a web-based metabolomics tool for pathway analysis and visualization. Bioinformatics 26:2342-2344.

19. Katsyuba E, Romani M, Hofer D, Auwerx J. 2020. NAD(+) homeostasis in health and disease. Nat Metab 2:9-31.

20. Xie N, Zhang L, Gao W, Huang C, Huber PE, Zhou X, Li C, Shen G, Zou B. 2020. NAD(+) metabolism: pathophysiologic mechanisms and therapeutic potential. Signal Transduct Target Ther 5:227.

21. Yaku K, Okabe K, Gulshan M, Takatsu K, Okamoto H, Nakagawa T. 2019. Metabolism and biochemical properties of nicotinamide adenine dinucleotide (NAD) analogs, nicotinamide guanine dinucleotide (NGD) and nicotinamide hypoxanthine dinucleotide (NHD). Sci Rep 9:13102.

22. Sharma R, Hartman TE, Beites T, Kim JH, Eoh H, Engelhart CA, Zhu L, Wilson DJ, Aldrich CC, Ehrt S, Rhee KY, Schnappinger D. 2023. Metabolically distinct roles of NAD synthetase and NAD kinase define the essentiality of NAD and NADP in *Mycobacterium tuberculosis*. mBio 14:e00340-23.

23. Bhat SA, Iqbal IK, Kumar A. 2016. Imaging the NADH:NAD(+) homeostasis for understanding the metabolic response of *Mycobacterium* to physiologically relevant stresses. Front Cell Infect Microbiol 6:145.

24. Darwin KH, Stanley SA. 2022. The aldehyde hypothesis: metabolic intermediates as antimicrobial effectors. Open Biol 12:220010.

25. Limón G, Samhadaneh NM, Pironti A, Darwin KH. 2023. Aldehyde accumulation in *Mycobacterium tuberculosis* with defective proteasomal degradation results in copper sensitivity. mBio 14:e00363-23.

26. Becker SH, Darwin KH. 2017. Bacterial proteasomes: mechanistic and functional insights. Microbiol Mol Biol Rev 81:e00036-16.

27. Samanovic MI, Tu S, Novak O, Iyer LM, McAllister FE, Aravind L, Gygi SP, Hubbard SR, Strnad M, Darwin KH. 2015. Proteasomal control of cytokinin synthesis protects *Mycobacterium tuberculosis* against nitric oxide. Mol Cell 57:984-994.

28. Tao X, Zhu Y, Diaz-Perez Z, Yu SH, Foley JR, Stewart TM, Casero RA, Jr., Steet R, Zhai RG. 2022. Phenylbutyrate modulates polyamine acetylase and ameliorates Snyder-Robinson syndrome in a Drosophila model and patient cells. JCI Insight 7:e158457.

29. Ahrens LA, Vonwil D, Christensen J, Shastri VP. 2017. Gelatin device for the delivery of growth factors involved in endochondral ossification. PLoS One 12:e0175095.

30. Gouzy A, Poquet Y, Neyrolles O. 2014. Nitrogen metabolism in *Mycobacterium tuberculosis* physiology and virulence. Nat Rev Microbiol 12:729-737.

31. Rhee KY, Erdjument-Bromage H, Tempst P, Nathan CF. 2005. S-nitroso proteome of *Mycobacterium tuberculosis*: enzymes of intermediary metabolism and antioxidant defense. Proc Natl Acad Sci U S A 102:467-472.

32. Richard-Greenblatt M, Bach H, Adamson J, Pena-Diaz S, Li W, Steyn AJC, Av-Gay Y. 2015. Regulation of ergothioneine biosynthesis and its effect on *Mycobacterium tuberculosis* growth and infectivity. J Biol Chem 290:23064-23076.

33. Buchmeier N, Fahey RC. 2006. The mshA gene encoding the glycosyltransferase of mycothiol biosynthesis is essential in *Mycobacterium tuberculosis* Erdman. FEMS Microbiol Lett 264:74-79.

34. Cheah IK, Halliwell B. 2012. Ergothioneine; antioxidant potential, physiological function and role in disease. Biochim Biophys Acta 1822:784-793.

35. Samanovic MI, Hsu HC, Jones MB, Jones V, McNeil MR, Becker SH, Jordan AT, Strnad M, Xu C, Jackson M, Li H, Darwin KH. 2018. Cytokinin signaling in *Mycobacterium tuberculosis*. mBio 9:e00989-18.

36. Biernacki T, Sandi D, Bencsik K, Vecsei L. 2020. Kynurenines in the pathogenesis of multiple sclerosis: therapeutic perspectives. Cells 9:1564.

37. Parish T, Stoker NG. 2000. Use of a flexible cassette method to generate a double unmarked *Mycobacterium tuberculosis tlyA* plcABC mutant by gene replacement. Microbiology 146:1969–1975.

38. San KY, Bennett GN, Berrios-Rivera SJ, Vadali RV, Yang YT, Horton E, Rudolph FB, Sariyar B, Blackwood K. 2002. Metabolic engineering through cofactor manipulation and its effects on metabolic flux redistribution in *Escherichia coli*. Metab Eng 4:182-192.

Table, Figures, and Supplemental Table and Figures

Table 1. MetPa Analysis of metabolite pathways altered in △*melH* compared to WT *Mm*[a]

KEGG Pathway Name[b]	Total[c]	Hits	*P*-value[d]	Impact
Pyrimidine metabolism	39	17	2.57E-08	0.511
Purine metabolism	65	22	5.29E-08	0.367
Glyoxylate and dicarboxylate metabolism	32	13	3.40E-06	0.362
Pyruvate metabolism	22	10	1.50E-05	0.485
Alanine, aspartate and glutamate metabolism	28	11	2.98E-05	0.763
Citrate cycle (TCA cycle)	20	9	4.59E-05	0.456
Glycolysis / Gluconeogenesis	26	10	8.70E-05	0.39
Arginine biosynthesis	14	7	1.51E-04	0.406
Nicotinate and nicotinamide metabolism	15	7	2.60E-04	0.461
Arginine and proline metabolism	38	11	6.91E-04	0.384

Pentose phosphate pathway	22	8	7.22E-04	0.296
Histidine metabolism	16	6	0.00291	0.344
Glycerolipid metabolism	16	6	0.00291	0.386
Glycine, serine and threonine metabolism	33	9	0.0034	0.128
Riboflavin metabolism	4	3	0.0035	0.5
Glutathione metabolism	28	8	0.00418	0.086
Glycerophospholipid metabolism	36	9	0.00639	0.532
Butanoate metabolism	15	5	0.01163	0
beta-Alanine metabolism	21	6	0.01298	0.056
Nitrogen metabolism	6	3	0.01508	0
D-Glutamine and D-glutamate metabolism	6	3	0.01508	0.5
Tryptophan metabolism	41	8	0.042441	0.05583

[a]Metabolic pathway analysis (MetPA), combining pathway enrichment analysis (*P* values) and pathway topology analysis (pathway impact) across all five carbon sources tested to identify which specific metabolic pathways are significantly altered. [b]Metabolites identified to have significant abundance differences between WT and Δ*melH Mm* were analyzed with

MetaboAnalyst 5.0 (https://www.metaboanalyst.ca/MetaboAnalyst/) to elucidate which pathways were changed upon mutation. [c]The total/maximum importance of each pathway = 1; pathway impact value = cumulative % from the matched metabolic nodes. [d]Pathways with the most significant change ($P < 0.05$) are presented.

Figures

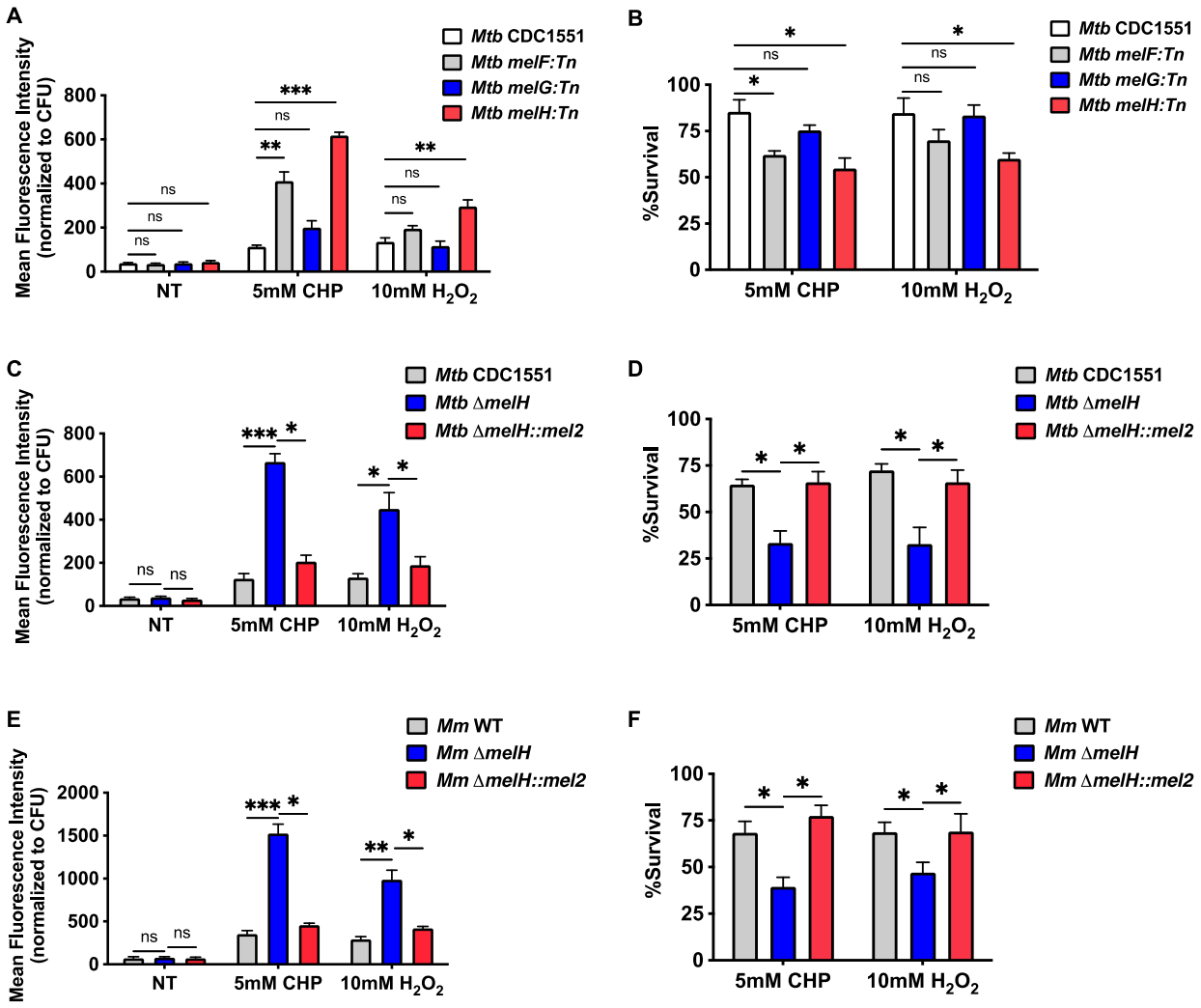

Figure 1. *melH* deletion exacerbates effect of and increases susceptibility to oxidative stress.

(A) Mean fluorescence intensity of CellROX Green (an ROS-sensitive dye) in WT *Mtb* (CDC1551) and *melF/G/H* transposon mutants treated with CHP or H_2O_2. NT, no treatment. (B) Percentage survival of WT and mutant *Mtb* strains determined by measuring bacterial CFU counts after a 30-min treatment with CHP or H_2O_2 in Middlebrook 7H9 medium containing glycerol as a single carbon source. (C) Mean fluorescence intensity of CellROX Green in WT

Mtb the Δ*melH* mutant, and the Δ*melH* complemented strain (*melH*::*mel2*) in 7H9 medium containing glycerol as a single carbon source. (D) Percentage survival of *Mtb* determined by measuring bacterial CFU counts after a 30-min treatment with CHP or H_2O_2 in 7H9 medium containing glycerol as a single carbon source. *P* values were determined by one-way analysis of variance using GraphPad Prism: $^{*}P < 0.05$, $^{**}P < 0.01$, $^{***}P < 0.001$; ns, not significant. Error bars indicate standard deviations of three replicate experiments.

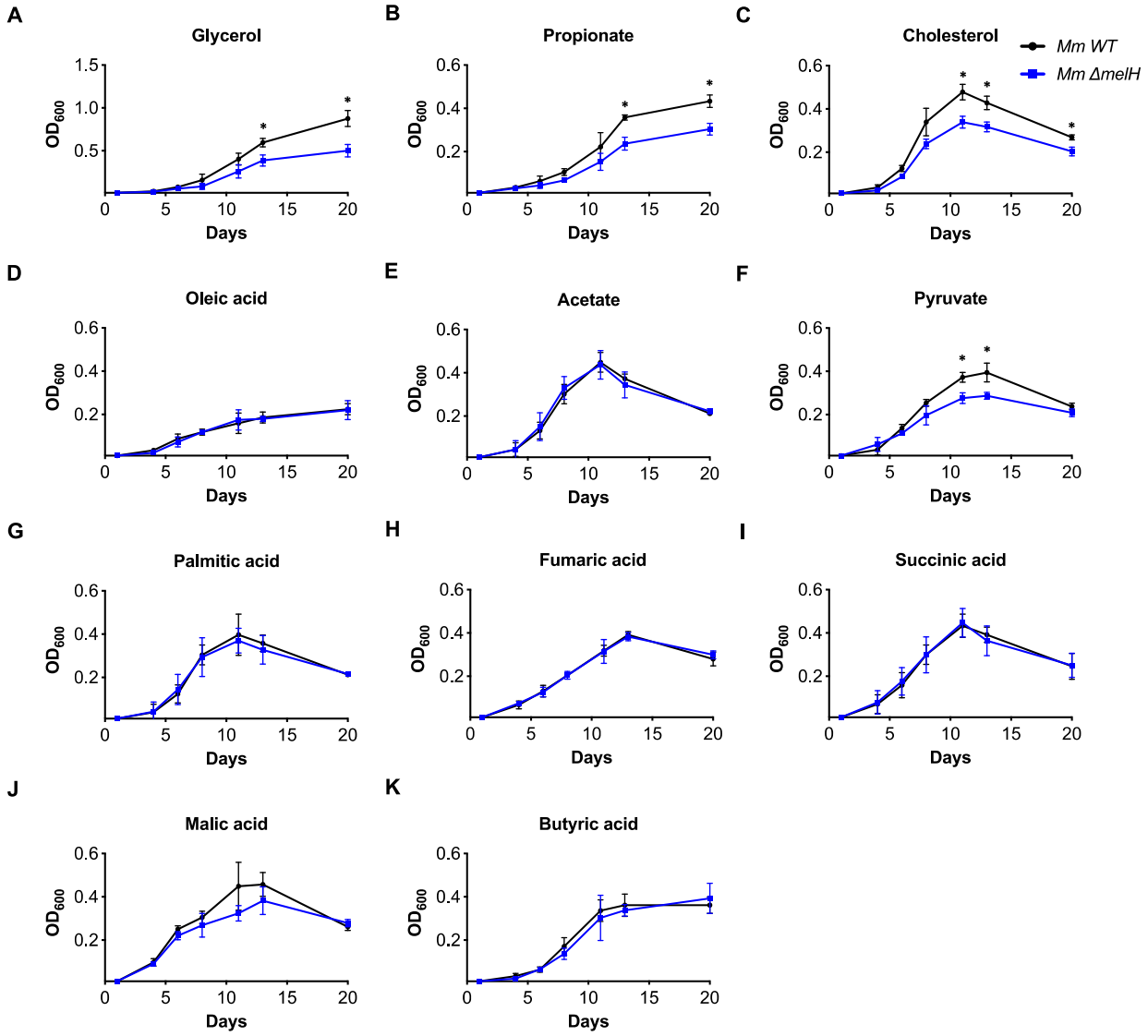

Figure 2. Effect of *melH* deletion on *Mm* growth rate depends on carbon source.

Growth rates of WT *Mm* (black lines) and the Δ*melH Mm* mutant (blue lines) in minimal medium containing either (A) glycerol, (B) propionate, (C) cholesterol, (D) oleic acid, (E) acetate, (F) pyruvate, (G) palmitic acid, (H) fumaric acid, (I) succinic acid, (J) malic acid, or (K) butyric acid as a single carbon source. *P* values were determined by one-way analysis of variance using GraphPad Prism: $*P < 0.05$, $**P < 0.01$. Error bars indicate standard deviations of three replicate experiments.

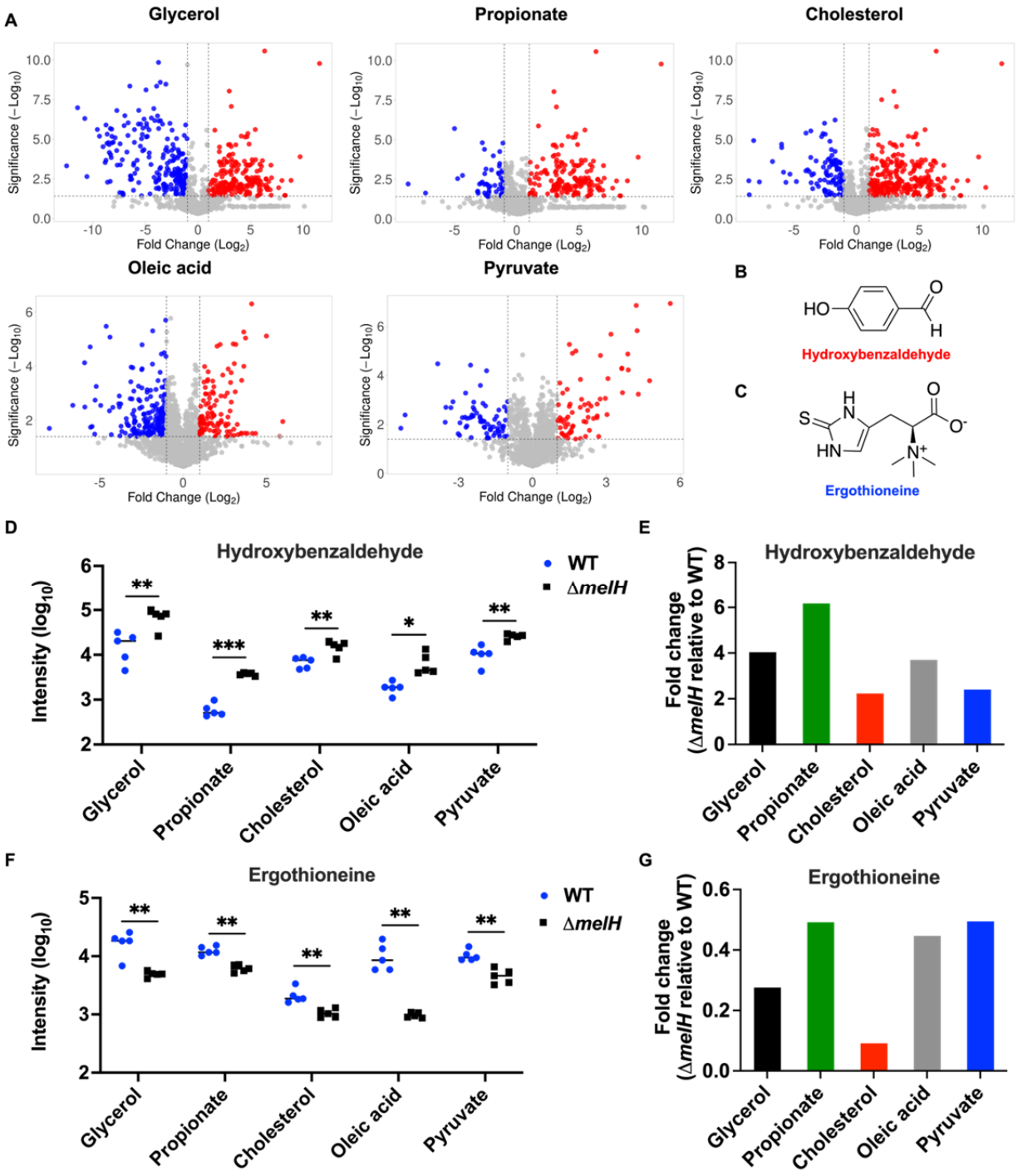

Figure 3. Liquid chromatography–mass spectrometry analysis of Δ*melH Mm* metabolites demonstrates increased *p*HBA levels and decreased EGT levels.

(A) Volcano plots showing fold change versus significance for metabolites extracted from WT and Δ*melH Mm* strains cultured with glycerol, propionate, cholesterol, oleic acid, or pyruvate as the sole carbon source. Fold change of metabolite abundance in Δ*melH Mm* relative to the abundance in the WT. Red and blue dots indicate metabolites with ≥ 2.0-fold increase or decrease, respectively, on the *x*-axis and a corrected *P* value of <0.05 ($-\log^{10} > 1.3$), on the y-axis; gray dots indicate metabolites with a <2.0-fold change and/or a *P* value of ≥ 0.05. (B and C) Chemical structures of (B) *p*HBA and (C) EGT. (D) Corresponding *p*HBA levels of in Δ*melH Mm* ($N = 5$) relative to WT ($N = 5$). *P* values were determined by one-way analysis of variance using GraphPad Prism: $*P < 0.05$, $**P < 0.01$, $***P < 0.001$. (E) Fold change of EGT levels in Δ*melH Mm* relative to the level in the WT. (F) Corresponding EGT levels of in Δ*melH Mm* ($N = 5$) relative to WT ($N = 5$). *P* values were determined by one-way analysis of variance using GraphPad Prism: $*P < 0.05$, $**P < 0.01$, $***P < 0.001$. (G) Fold change of EGT levels in Δ*melH Mm* relative to the level in the WT.

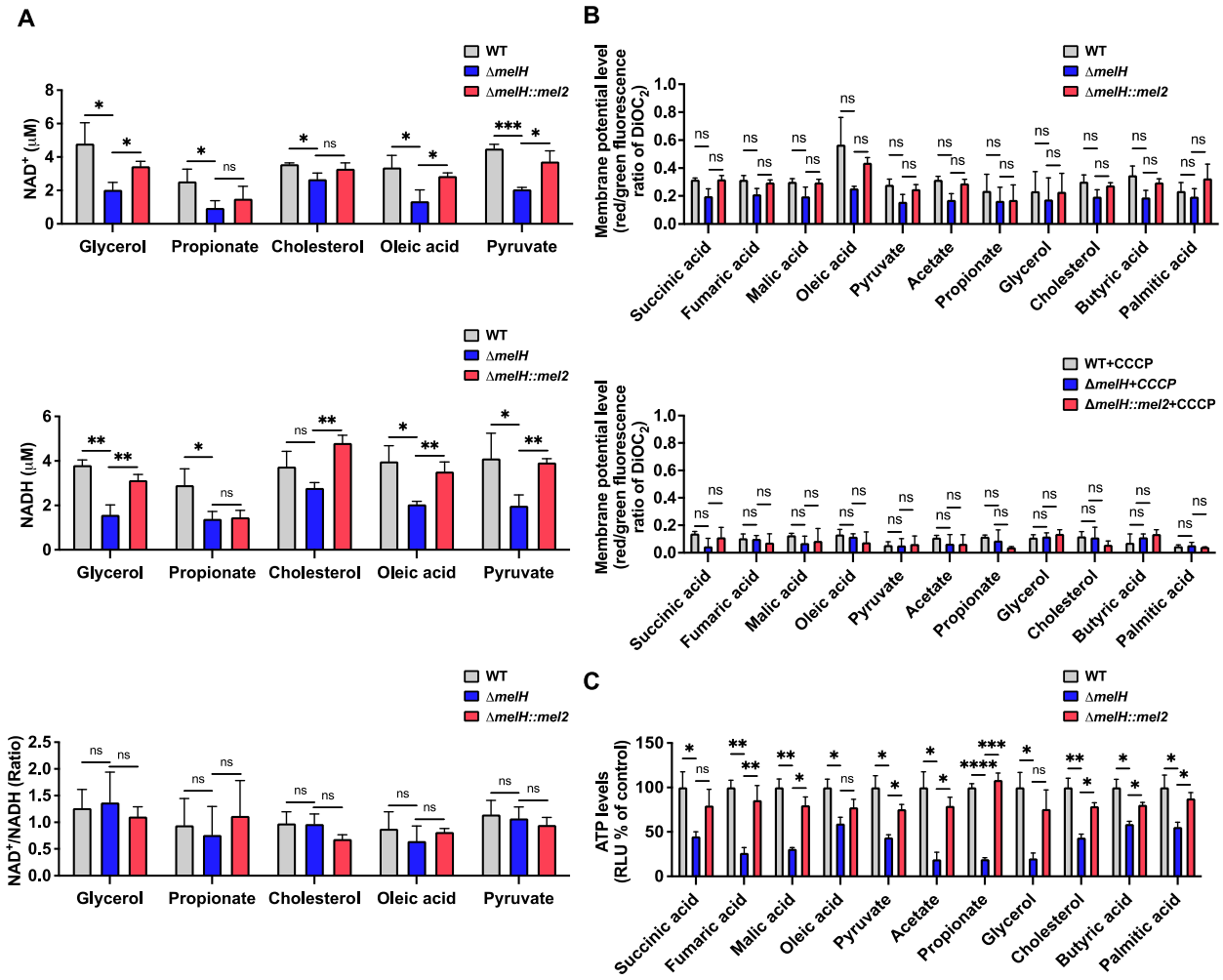

Figure 4. Deletion of *melH* reduces intracellular ATP levels and NAD^+ and NADH concentrations in *Mm*.

(A) Intracellular NAD^+ and NADH concentrations in WT, Δ*melH*, and Δ*melH* complemented (*melH*::*mel2*) strains of *Mm*, as measured via recycling assays, along with calculated NAD^+/NADH ratios. (B) Bacterial membrane potentials, measured with a BacLightTM Membrane Potential kit, for WT, Δ*melH*, and *melH*::*mel2 Mm* cultured with succinic acid, fumaric acid, malic acid, oleic acid, pyruvate, acetate, propionate, glycerol, cholesterol, butyric acid, or palmitic acid as the sole carbon source. $DiOC_2$ = 3,3′-diethyloxacarbocyanine iodide. (C)

Intracellular ATP levels, as measured by means of the luciferase/luciferin system, in WT, Δ*melH*, and *melH*::*mel2 Mm* cultured with succinic acid, fumaric acid, malic acid, oleic acid, pyruvate, acetate, propionate, glycerol, cholesterol, butyric acid, or palmitic acid as the sole carbon source. *P* values were determined by one-way analysis of variance using GraphPad Prism: $*P < 0.05$, $**P < 0.01$, $***P < 0.001$. Error bars indicate standard deviations of three replicate experiments.

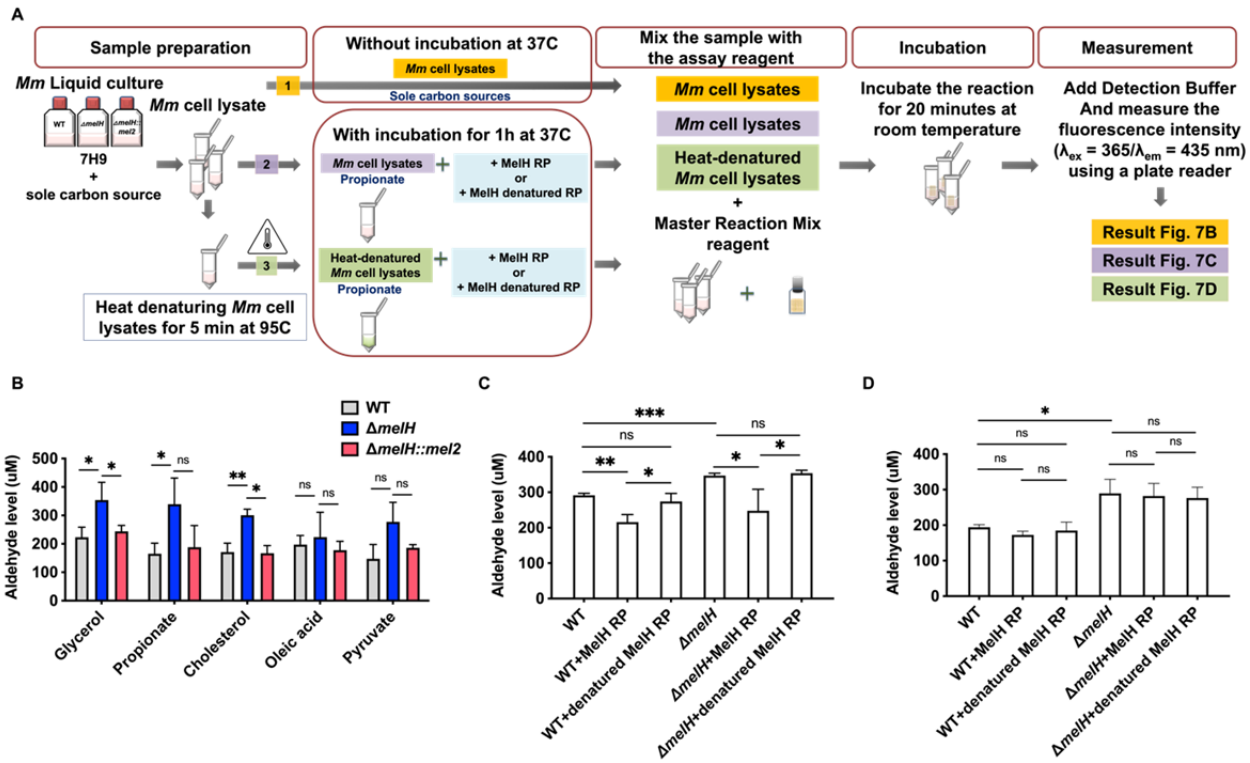

Figure 5. Disruption of *melH* causes intracellular aldehyde accumulation.

(A) Workflow of aldehyde measurement. (B) Aldehyde concentrations in WT, Δ*melH*, and Δ*melH* complemented (*melH*::*mel2*) strains of *Mm* cultured with glycerol, propionate, cholesterol, oleic acid, or pyruvate as the sole carbon source. Aldehyde concentrations were determined with a fluorometric assay kit. After the mycobacteria were incubated with the aldehyde detection reagent for 30 min, the absorbance of the supernatants at 405 nm was measured using a plate reader. (C) Aldehyde concentrations in WT and Δ*melH Mm* lysates incubated with MelH recombinant protein or denatured MelH recombinant protein for 1 hour. (D) Aldehyde concentrations in enzyme-denatured WT and Δ*melH Mm* lysates incubated with MelH recombinant protein or denatured MelH recombinant protein for 1 hour. *P* values were determined by one-way analysis of variance using GraphPad Prism: $*P < 0.05$, $**P < 0.01$, $***P < 0.001$; ns, not significant. Error bars indicate mean ± SD ($N = 3$ independent experiments).

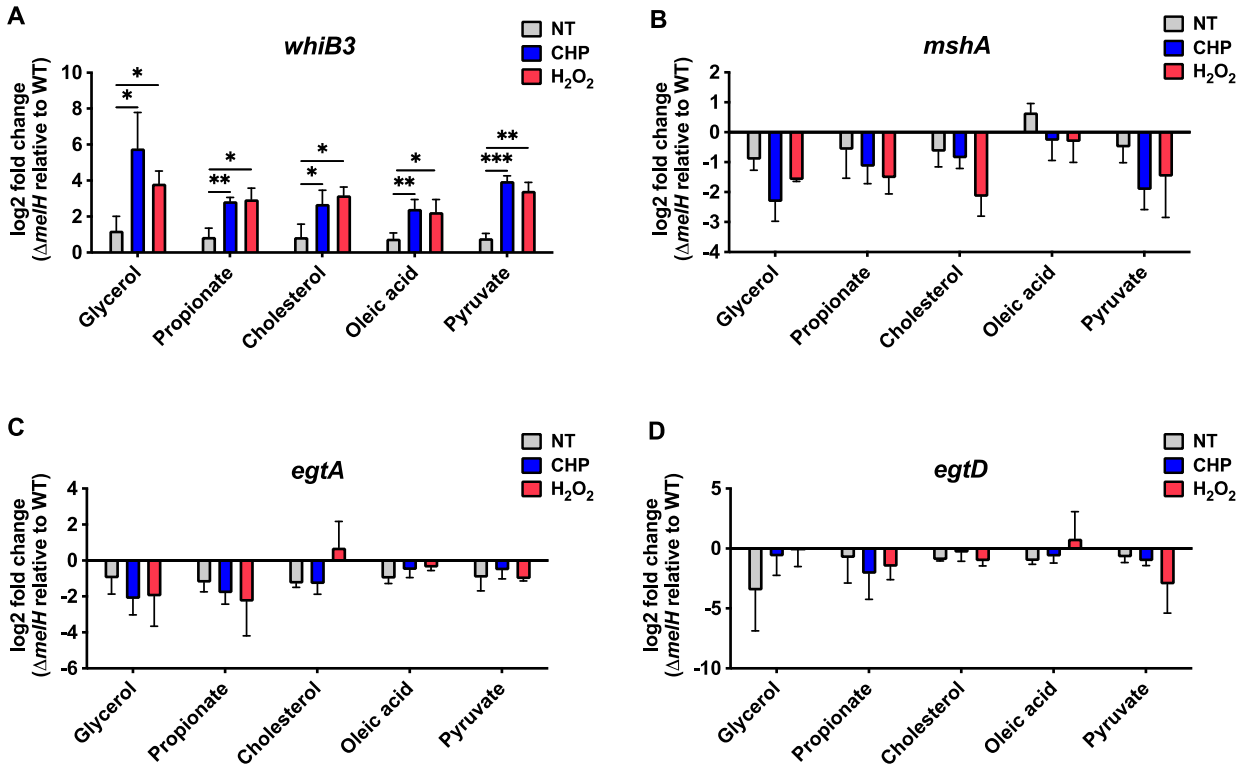

Figure 6. *melH* deletion affects expression of *whiB3* and EGT and MSH biosynthesis genes (*egtA*, *egtD*, and *mshA*) in *Mm* in response to oxidative stress.

Comparison of (A) *whiB3*, (B) *mshA*, (C) *egtA*, and (D) *egtD* expression in CHP- and H_2O_2-treated *Mm*. NT, no treatment. Total RNA was extracted from the bacteria, and intracellular gene expression was measured by quantitative real-time PCR. *P* values were determined by one-way analysis of variance using GraphPad Prism: $*P < 0.05$, $**P < 0.01$, $***P < 0.001$. Error bars indicate standard deviations of three replicate experiments.

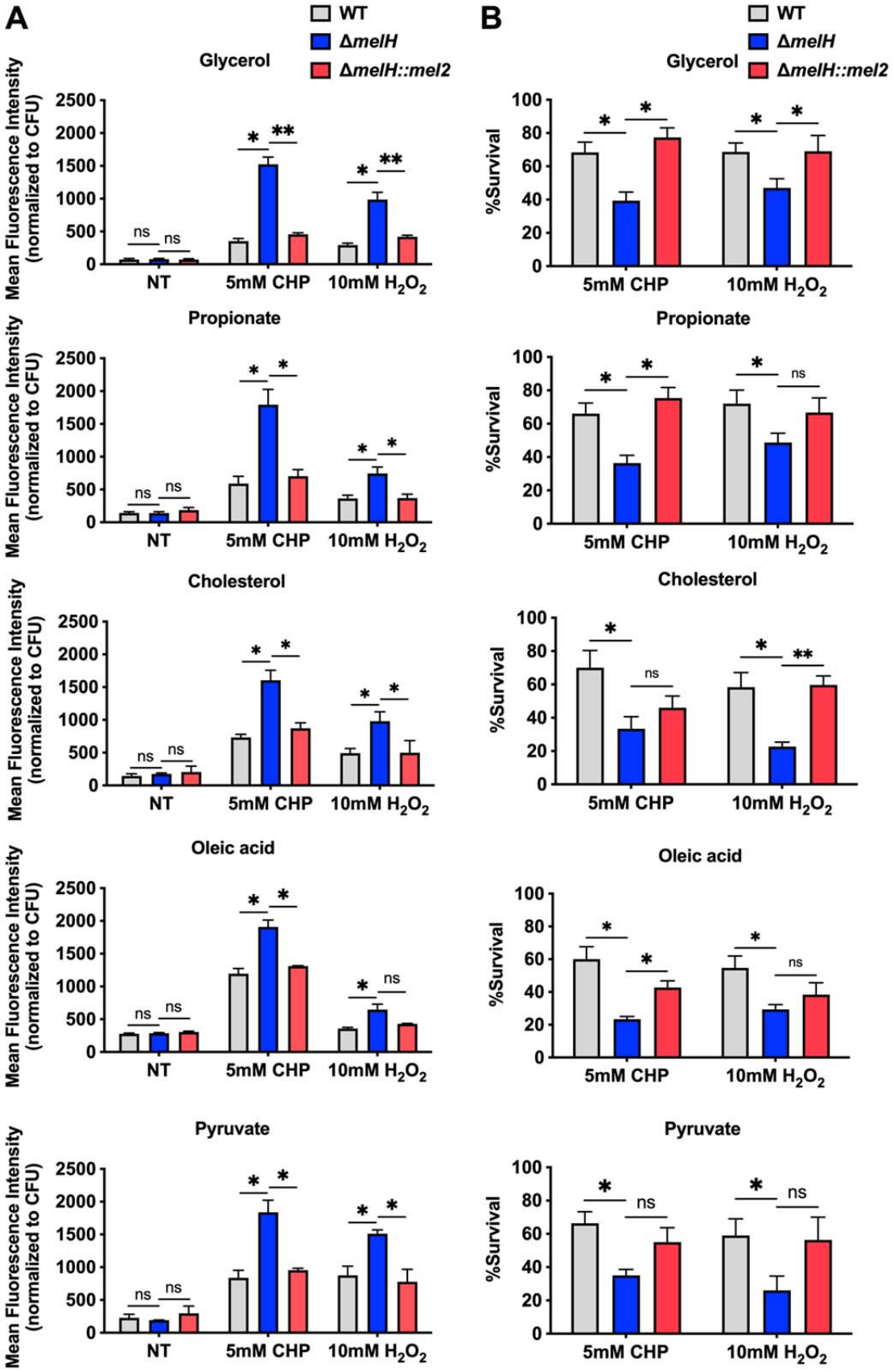
A
WT
ΔmelH
ΔmelH::mel2
Glycerol
Propionate
Cholesterol
Oleic acid
Pyruvate
Mean Fluorescence Intensity (normalized to CFU)
NT
5mM CHP
10mM H2O2
B
%Survival
ns
*
**

Figure 7. Absence of *melH* in *Mm* results in heightened vulnerability to oxidative stress in response to carbon catabolism.

(A) Mean fluorescence intensity of CellROX Green (an ROS-sensitive dye) CHP- or H_2O_2-treated WT, Δ*melH*, and Δ*melH* complemented (*melH*::*mel2*) strains of *Mm* cultured in 7H9 medium with glycerol, propionate, cholesterol, oleic acid, or pyruvate as the sole carbon source. (B) Percentage survival of WT, Δ*melH*, and *melH*::*mel2* strains of *Mm* determined by measuring bacterial CFU counts after a 30-min treatment with CHP or H_2O_2 in 7H9 medium containing glycerol, propionate, cholesterol, oleic acid, or pyruvate as a single carbon source. *P* values were determined by one-way analysis of variance using GraphPad Prism: $^*P < 0.05$, $^{**}P < 0.01$, $^{***}P < 0.001$; ns, not significant. Error bars indicate standard deviations of three replicate experiments.

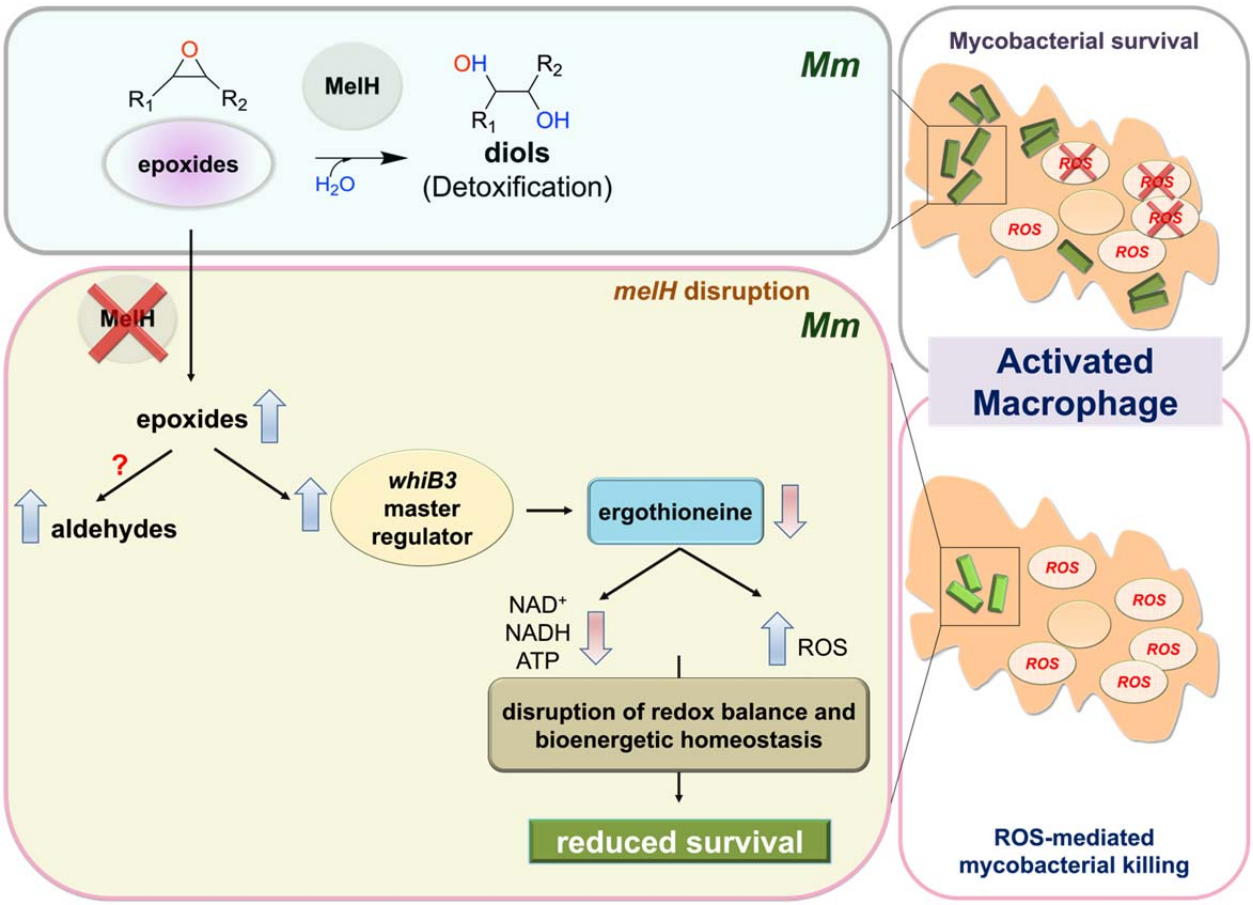

Figure 8. Model for metabolic consequences of *melH* deficiency.

In *Mtb* and *Mm*, *melH* encodes epoxide hydrolase b (MelH), which catalyzes hydrolysis of epoxides formed in the ROS detoxification process and aids mycobacterial survival within host macrophages. However, in the absence of functional MelH in the Δ*melH* mutant, there is an accumulation of epoxides or their precursors, leading to the buildup of aldehydes. The deletion of *melH* results in elevated expression of *whiB3* and decreased production of the redox buffer EGT. In addition, *melH* causes a decrease in intracellular levels of NAD^+, NADH, and ATP. All of these changes affect bioenergetic homeostasis and bacterial growth and ultimately sensitize the mutant to oxidative stress.

Table S1. List of oligonucleotide sequences used as primers in this study

Primer name	Sequence 5'-3'	Description
hygromycin cassette F	ATATATCATATGATAACTTCGTATAATGTATG CTATACGAAGTTATGGATCATC	For hygromycin cassette cloning
hygromycin cassette R	ATATATAAGCTTATAACTTCGTATAGCATACA TTATACGAAGTTATAAGCTGG	For hygromycin cassette cloning
***Mtb _melH*_F**	ATAACATATGGTGTCGCAGGTCCATCG	For *Mtb melH* pretein expression
***Mtb _melH*_R**	ATAAAAGCTTTCACGGCCGCAGC	For *Mtb melH* pretein expression
***Mm_whiB3*_F**	GCAGTTGCAGGGCCTAT	For *Mm whiB3* gene expression
***Mm _whiB3*_R**	TTGAGCAGCAGGTCACG	For *Mm whiB3* gene expression
***Mm _egtA*_F**	CCGACCATGCGGATCAAT	For *Mm egtA* gene expression
***Mm _egtA*_R**	GCTATCTGGACAGTCTTTCCG	For *Mm egtA* gene expression
***Mm _egtD*_F**	CCGCCCAAATGGTTCTATGA	For *Mm edtD* gene expression
***Mm _egtD*_R**	TAGGCGTCCACGTTGAAATC	For *Mm egtD* gene

		expression
***Mm _mshA*_F**	TTCGAGGGTCTGGACAAGTA	For *Mm mshA* gene expression
***Mm _mshA*_R**	ACAGCCAATAGTGCGAGTG	For *Mm mshA* gene expression

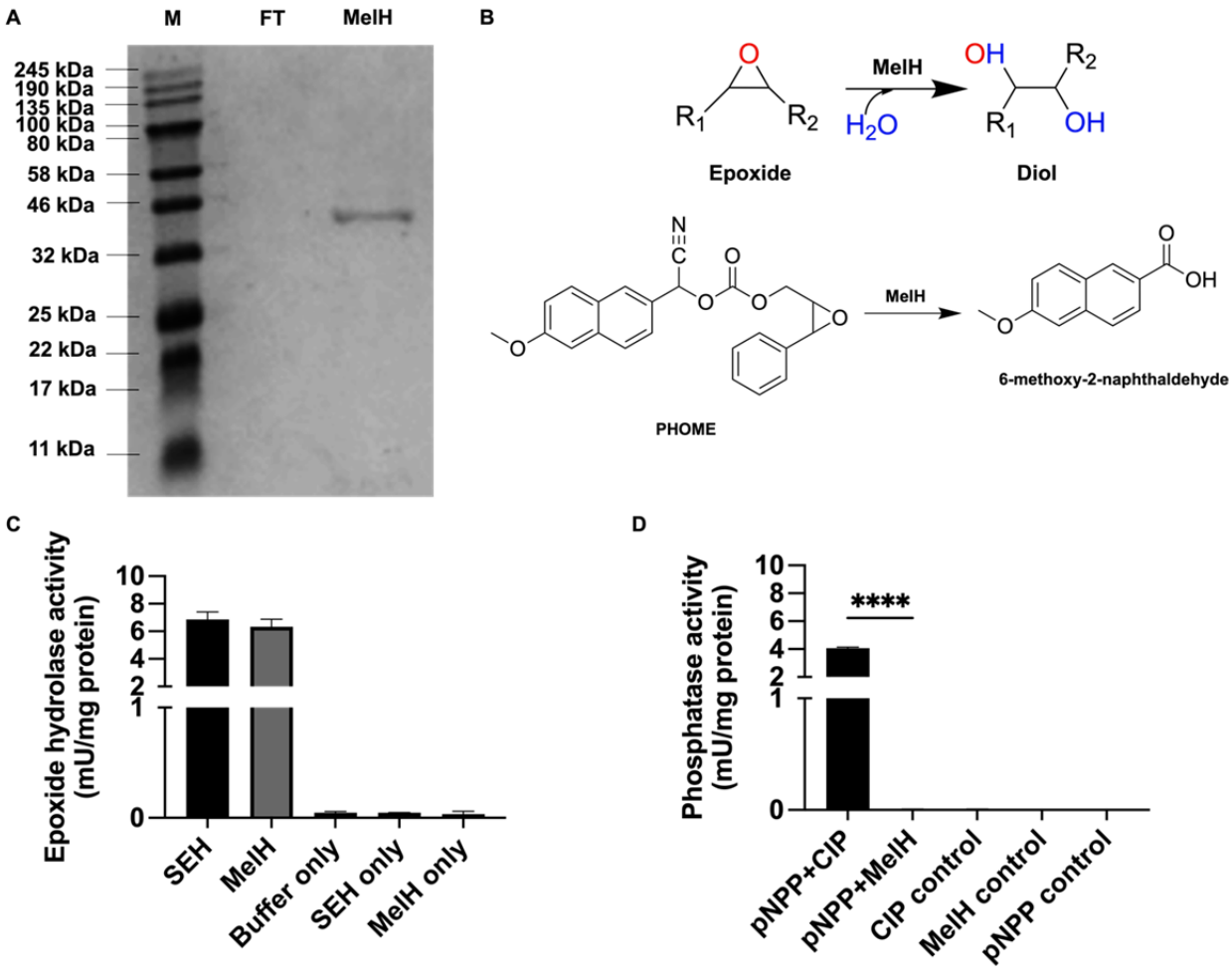

Figure S1. Enzyme encoded by *melH* has epoxide hydrolase activity.

(A) SDS-PAGE analysis of recombinant protein production in *Escherichia coli* BL21(DE3) pET28b-EphB$_{Mtb}$. A 6-His-tagged MelH (~40 kDa) recombinant protein was purified by Ni-nitrilotriacetic acid affinity and size-exclusion chromatography; and a protein marker (M), a flow-through control (FT), and MelH protein (MelH) were loaded onto the gel. (B) Reaction catalyzed by MelH and hydrolysis of artificial substrate PHOME, which was used for the

epoxide hydrolase assay. (C) Epoxide hydrolase activity for sEH (positive control) and MelH (D) Analysis of alkaline phosphatase activity of calf intestinal alkaline phosphatase (CIP, control) and MelH. The substrate was *para*-nitrophenyl phosphate (pNPP), a generic phosphatase substrate whose dephosphorylated product, *para*-nitrophenol (pNP), is intensely yellow under alkaline conditions and absorbs at 405 nm. *P* values were determined by one-way analysis of variance using GraphPad Prism: ****$P < 0.0001$. Error bars indicate standard deviations of three replicate experiments.

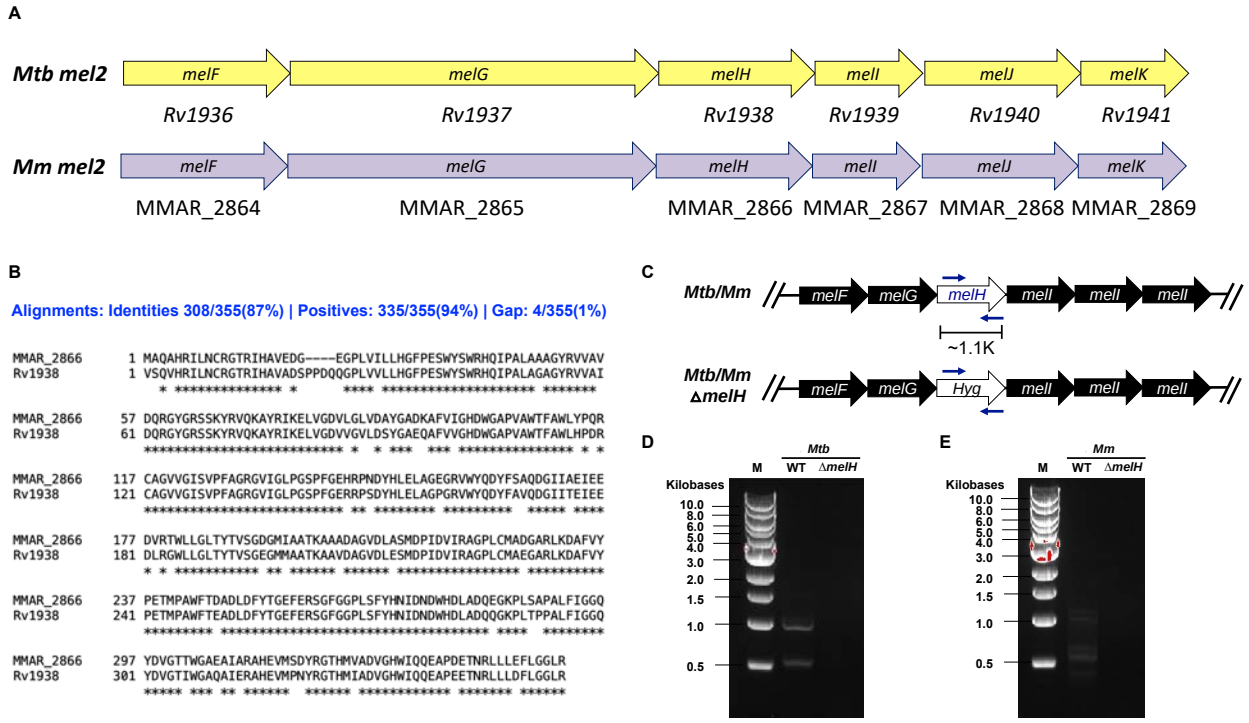

Figure S2. Similarity of *Mtb melH* to *Mm melH*.

(A) Schematic representation of the chromosomal region containing the *mel* genes of *mel2 loci* in *Mtb* and *Mm*. (B) The protein BLAST (BLASTp) sequence alignments of Mtb *Rv1938*-encoded MelH amino acid sequence with the amino acid sequence of Mm MMAR_2866-encoded MelH, revealed 87% identities, 94% positives, and 1% gap. (C) Schematic representation of *Mtb* and *Mm* genomic region containing *melH*, indicating the location of the primers used to validate allelic exchange and gene deletion of *melH*. (D) Validation of *Mtb melH* deleted mutant (Δ*melH* mutant) showing the PCR product amplimied by *melH* primers. (E) Validation of *Mm melH* deleted mutant (Δ*melH* mutant) showing the PCR product amplimied by *melH* primers.

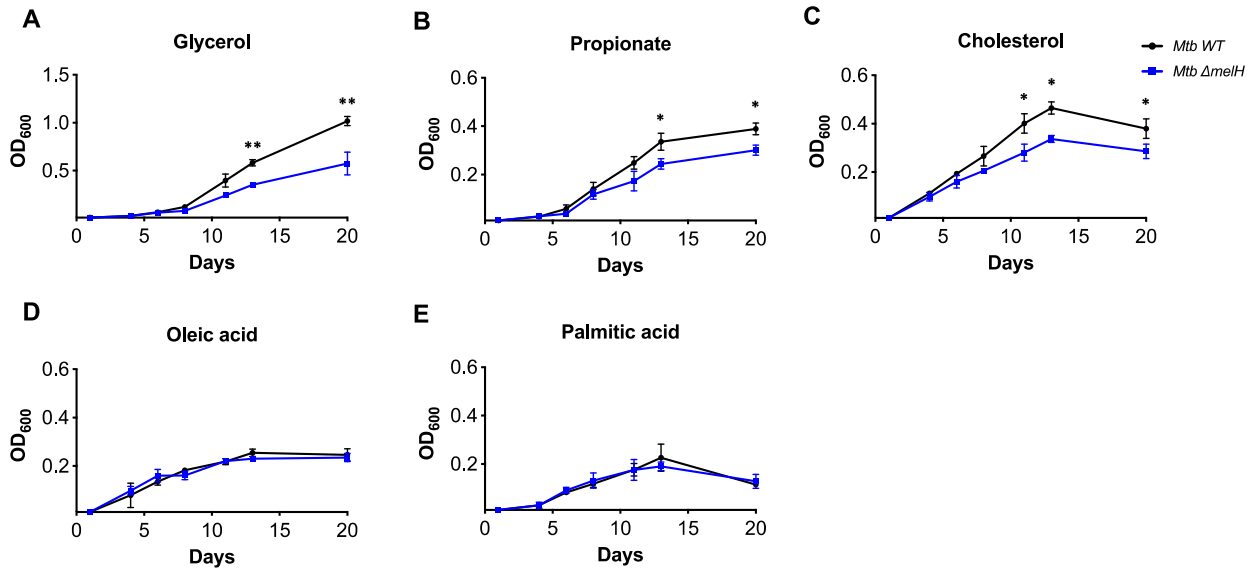

Figure S3. Effect of *melH* deletion on *Mtb* growth rate depends on carbon source.

Growth rates of WT *Mtb* (black lines) and the Δ*melH Mtb* mutant (blue lines) in minimal medium containing either (A) glycerol, (B) propionate, (C) cholesterol, (D) oleic acid, or (E) palmitic acid as a single carbon source. *P* values were determined by one-way analysis of variance using GraphPad Prism: $*P < 0.05$, $**P < 0.01$. Error bars indicate standard deviations. of three replicate experiments.

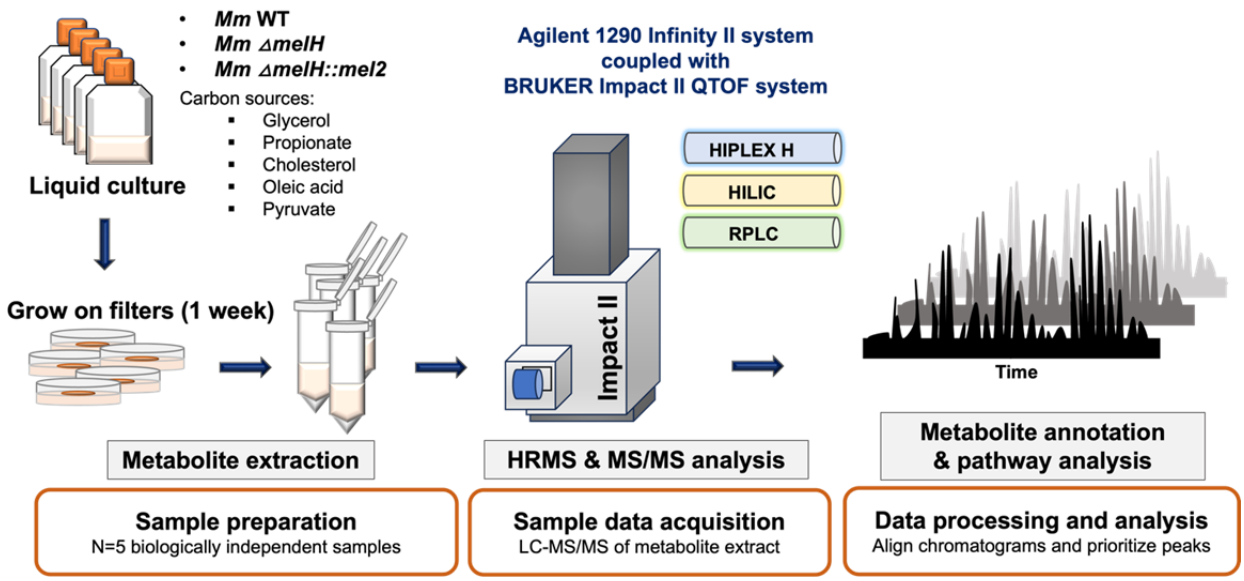

Figure S4. Workflow and metabolite data analysis using untargeted metabolomic analysis.

Overview of global, untargeted metabolomic workflow.

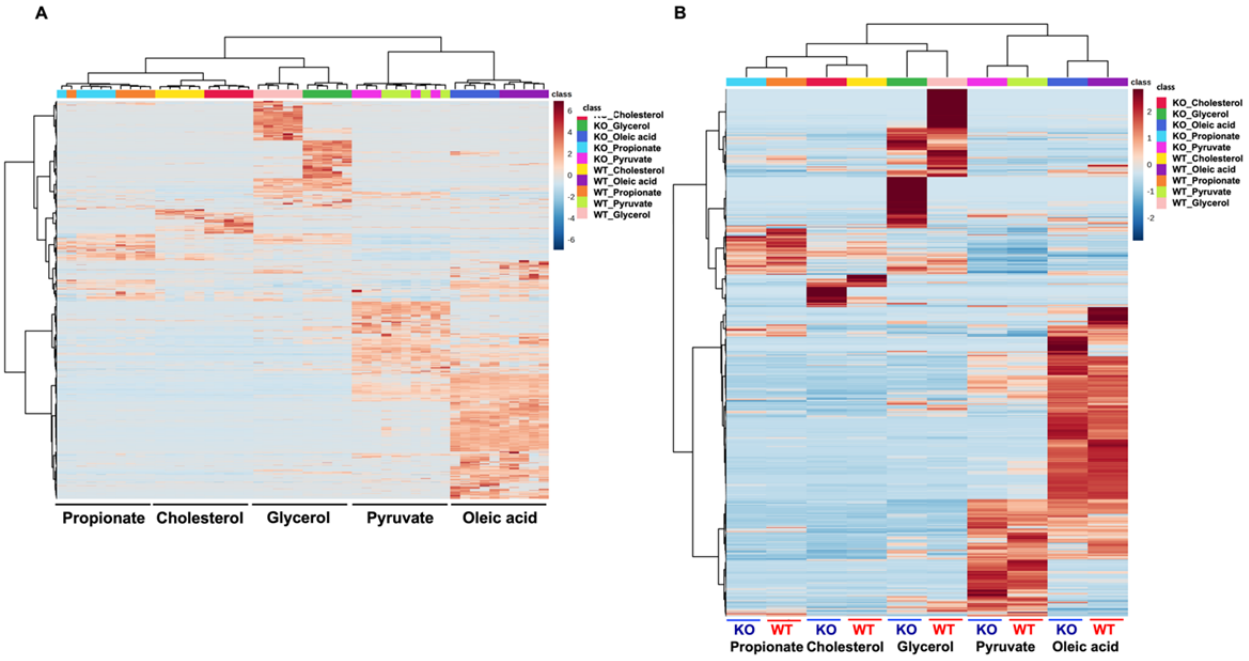

Figure S5. Liquid chromatography–mass spectrometry analysis of putative metabolites in *Mm* demonstrates distinct metabolic differences in response to carbon catabolism.

(A) Heat map showing ratios of metabolite concentrations in individual cell extracts prepared from Δ*melH Mm* ($N = 5$) versus concentrations in WT *Mm* ($N = 5$) cultured in the presence of glycerol, propionate, cholesterol, oleic acid, or pyruvate. (B) Heat map showing average ratios ($N = 5$) of metabolite concentrations in Δ*melH* versus concentrations in the WT grown on glycerol, propionate, cholesterol, oleic acid, or pyruvate.

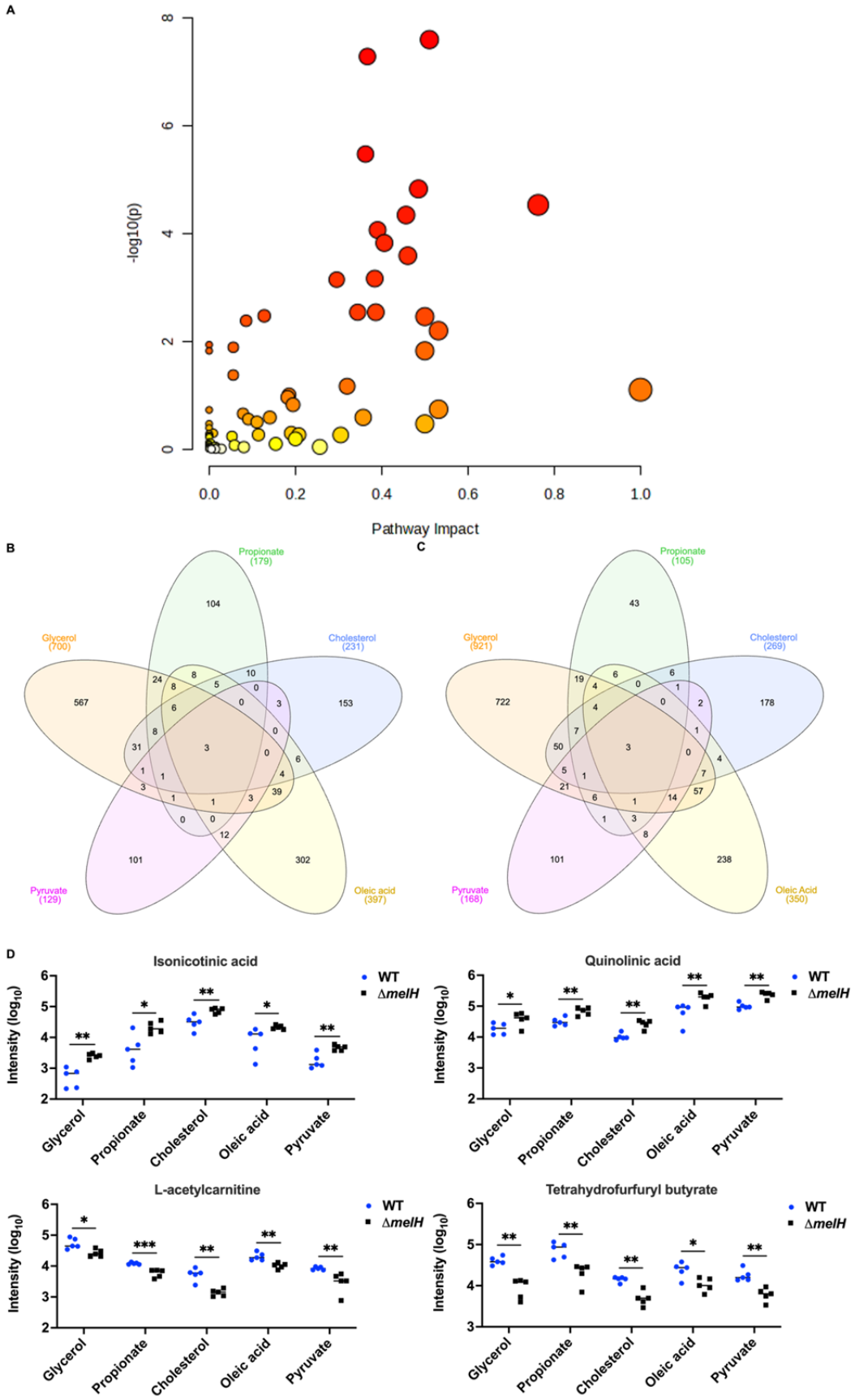
A
-log10(p)
Pathway Impact
B
Propionate (179)
Glycerol (700)
Cholesterol (231)
Pyruvate (129)
Oleic acid (397)
C
Propionate (105)
Glycerol (921)
Cholesterol (269)
Pyruvate (168)
Oleic Acid (350)
D
Isonicotinic acid
Quinolinic acid
L-acetylcarnitine
Tetrahydrofurfuryl butyrate
WT
ΔmelH
Intensity (log10)
Glycerol
Propionate
Cholesterol
Oleic acid
Pyruvate

Figure S6. Metabolomic analysis of *melH*-deficiency *Mm*.

(A) Untargeted metabolite profiling assessed by MetPa enrichment analysis, based on changes in the relative abundance of metabolites (see also Table S1), indicate that melH has a profound effect on Mm metabolism. (B) Venn diagram illustrating overlap of significantly increased metabolites (para-hydroxybenzaldehyde, Isonicotinic acid, Quinolinic acid) in Δ*melH Mm* grown with different carbon sources. (C) Venn diagram illustrating overlap of significantly decreased metabolites (L-acetylcarnitine, EGT, and tetrahydrofurfuryl butyrate) in Δ*melH Mm* grown with different carbon sources. (D) Corresponding levels of Isonicotinic acid, Quinolinic acid, L-acetylcarnitine, and tetrahydrofurfuryl butyrate in Δ*melH Mm* (N = 5) relative to WT (N = 5). *P* values were determined by one-way analysis of variance using GraphPad Prism: $^{*}P < 0.05$, $^{**}P < 0.01$, $^{***}P < 0.001$.

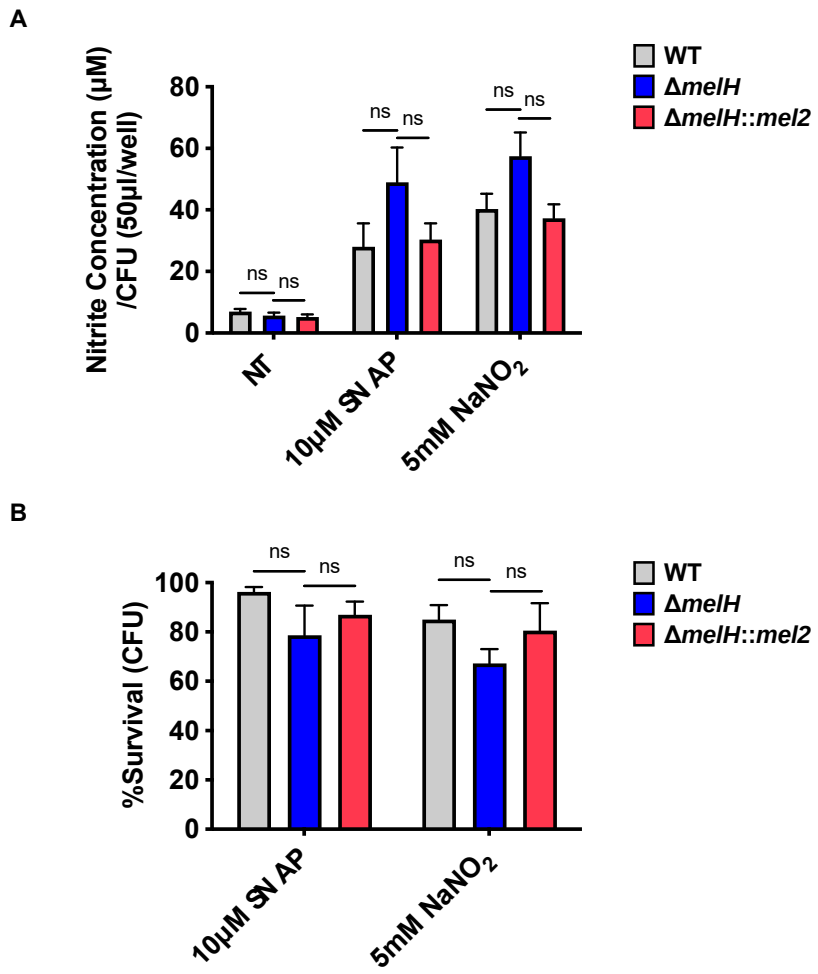

Figure S7. Impact of *melH* deletion on nitrite production in *Mm*.

(A) Nitrite production in WT, Δ*melH*, and Δ*melH* complemented (*melH*::*mel2*) strains of *Mm* grown in the presence of *S*-nitroso-*N*-acetylpenicillamine SNAP or $NaNO_2$ with propionate as the sole carbon source. The nitric oxide assay was conducted with the Griess reagent system. NT, no treatment. (B) Percentage survival of WT, Δ*melH*, and *melH*::*mel2 Mm* determined by measuring bacterial CFU counts after a 30-min treatment with SNAP or $NaNO_2$. *P* values were determined by one-way analysis of variance using GraphPad Prism; ns, not significant. Error bars indicate mean ± SD (*N* = 3 independent experiments).